

Article

An Improved Method for Swing State Estimation in Multirotor Slung Load Applications

Emanuele Luigi de Angelis *  and Fabrizio Giulietti 

Department of Industrial Engineering, Interdepartmental Centre for Industrial Aerospace Research, University of Bologna, 47121 Forlì, Italy; fabrizio.giulietti@unibo.it

* Correspondence: emanuele.deangelis4@unibo.it; Tel.: +39-0543-374-453

Abstract: A method is proposed to estimate the swing state of a suspended payload in multirotor drone delivery scenarios. Starting from the equations of motion of the coupled slung load system, defined by two point masses interconnected by a rigid link, a recursive algorithm is developed to estimate cable swing angle and rate from acceleration measurements available from an onboard Inertial Measurement Unit, without the need for extra sensors. The estimation problem is addressed according to the Extended Kalman Filter structure. With respect to the classical linear formulation, the proposed approach allows for improved estimation accuracy in both stationary and maneuvering flight. As an additional contribution, filter performance is enhanced by accounting for aerodynamic disturbance force, which largely affects the estimation accuracy in windy flight conditions. The validity of the proposed methodology is demonstrated as follows. First, it is applied to an octarotor platform where propellers are modeled according to blade element theory and the load is suspended by an elastic cable. Numerical simulations show that estimated swing angle and rate represent suitable feedback variables for payload stabilization, with benefits on flying qualities and energy demand. The algorithm is finally implemented on a small-scale quadrotor and is investigated through an outdoor experimental campaign, thus proving the effectiveness of the approach in a real application scenario.

Keywords: drone delivery; drone control system; multirotor; suspended load; swing state estimation; Extended Kalman Filter; swing damping



Citation: de Angelis, E.L.; Giulietti, F. An Improved Method for Swing State Estimation in Multirotor Slung Load Applications. *Drones* **2023**, *7*, 654. <https://doi.org/10.3390/drones7110654>

Academic Editor: Diego González-Aguilera

Received: 25 September 2023
Revised: 28 October 2023
Accepted: 29 October 2023
Published: 31 October 2023



Copyright: © 2023 by the authors. Licensee MDPI, Basel, Switzerland. This article is an open access article distributed under the terms and conditions of the Creative Commons Attribution (CC BY) license (<https://creativecommons.org/licenses/by/4.0/>).

1. Introduction

The use of drones for the transportation of loads is a topic of recent interest [1,2]. Both UPS and Amazon, for example, have projects to use drones for their deliveries, with solutions ranging from the adoption of manipulation devices to the equipment of ad hoc cargo compartments [3]. However, there is another field of load transportation that has scientific relevance, namely the use of unmanned rotary-wing platforms for transporting cable-suspended loads. In this respect, it is noted that multirotor vehicles exhibit complex dynamic behavior and the presence of a cable-suspended payload inherently increases the complexity of such systems because additional degrees of freedom are introduced. Moreover, if uncontrolled, a cable-suspended payload changes the dynamics of the flying vehicle and can result in an unstable system, with potential damage to the payload or its environment after collision with obstacles [4].

The problem of a single rotorcraft carrying a load has been addressed in the literature considering minimal load swing, with a number of works investigating different control approaches [5–18]. In [16], for example, the transportation problem is solved by an energy-based control strategy and a nonlinear feedback controller based on Linear Matrix Inequality (LMI). In [17], a Real-Time Dynamic Programming (RTDP) algorithm is proposed to optimize journey time and energy consumption. The RTDP algorithm is developed by discretizing the journey into distance interval horizons and applying the RTDP sweep to the

current horizon to obtain the optimal velocity decision. In [18], a path-tracking controller is developed based on existing Lyapunov-based path tracking control laws for free-flying aerial vehicles, which are further backstepped through the vehicle rotation dynamics.

In order to achieve anti-sway capabilities, the accurate measurement of load position information is fundamental, with solutions that are often inspired from bridge crane applications [19]. Typical methods include the use of motion capture systems, where accurate estimation comes at the cost of complex and expensive installations [20,21]. Although optical-based alternatives can be conceived, such as visual detection [22], they require extra sensor devices that cause growth in take-off weight and power consumption or sensitivity to environmental conditions [23].

Methods that are not based on the use of ad hoc camera installations rely on instrumentations that are fixed with respect to the load. It is the case of high-accuracy GNSS devices [24], whose application would be needed for both the drone and the load in outdoor scenarios. In [25], a novel method for measuring the sway angle by using a clinometer attached to the load is proposed. In [26], the use of potentiometers is suggested to estimate the orientation of appendages for aerial manipulation tasks, with the possibility to perform swing angle measurements of suspended rigid links. In [27], a swing angle estimation method is developed without any external sensors except an attached IMU module. First, the authors derive an estimation algorithm of the disturbance force caused by the slung load using a disturbance observer. Since the direction of the tension force is the same as the direction of the wire, the swing angle is directly estimated from force components. The limitations of the method are pointed out and discussed, based on the inherent difficulty to discriminate the load-induced forces from propulsive or other disturbance contributions. To this end, the authors suggest a practical alternative where a single load-cell is mounted on the tether. In a recent work by one of the authors of the present paper [28], a method is presented to estimate swing angles in multirotor applications, with no need to rely on extra sensors, except for the available accelerometers. Sensor readings and dynamic model information are combined by a Fading Gaussian Deterministic Filter (FGDF), based on a recursive linear formulation derived in [29]. The approach is validated by numerical simulations and filter performance is measured and optimized in the presence of model uncertainties and measurement errors. In a similar manner, two types of anti-sway trajectory generation methods are derived in [30] on a linear basis to provide dynamically feasible and optimal trajectories for the system. In such a work, the authors remarkably release the aggressive motion and the payload swing in the transient response, while a Kalman Filter (KF) is proposed to estimate payload state from onboard accelerometers and gyroscopes.

The contribution of the present paper is twofold: (1) a new formulation of the estimation procedure described in [28] is derived and implemented to overcome performance limitations related to model uncertainties and agile maneuver conditions. To this aim, the point mass equations of the coupled slung load system are first derived through the Lagrangian approach, based on the assumption of a mass-less and rigid cable, and an Extended Kalman Filter (EKF) structure is implemented to allow for improved estimation performance. Then, the state vector of the EKF is extended by including the three components of aerodynamic disturbance force. Such a strategy is adopted to enhance estimation performance in windy conditions and provide an accurate estimation of the overall thrust generated by the rotors, making the need of a load cell unnecessary. (2) As a further contribution, the estimated swing angles and rates are used in a proportional feedback control logic aiming at the stabilization of payload oscillations. A controller structure that stems from the idea in [15] is designed as an auxiliary contribution to available control loops specifically developed for rotorcraft GNC tasks and possibly shaped in an optimal control fashion [31]. As a byproduct, it is shown that, for the same mission, the activation of the payload stabilization controller noticeably reduces the energy required from the battery pack with respect to the case when trajectory-tracking only is performed.

In what follows, preliminary definitions and the point mass system dynamic model are provided in Section 2. EKF recursive equations are detailed in Section 3, where the

innovation vector is defined as the difference between model-based and measured vehicle accelerations, projected in the inertial frame. Validation is performed in Section 4. The proposed algorithm is first validated by means of numerical simulations. Mission tasks related to a real operational scenario are considered, where a battery-powered octarotor aircraft is modeled as a rigid body equipped with an elastic cable. System modeling includes electric propulsion system components and Blade Element characterization of propellers [32,33]. Environmental disturbances and model uncertainties are accounted and state estimation is evaluated during sample maneuvers, showing satisfactory accuracy for both swing state and aerodynamic disturbance characterization. The recursive estimation algorithm is then deployed on a commercial off-the-shelf Pixhawk controller, and filter performance is investigated for a small-scale quadrotor equipped with a two-axis potentiometer calibrated for direct measurement of cable swing angles. A comparison is thus provided between measured and estimated states for both the original FGDF of [28] and the updated EKF algorithm, the latter showing improved accuracy and robustness against windy conditions. A section of concluding remarks ends this paper.

2. System Modeling

Starting from the definition of reference frames, a 3 degrees-of-freedom mathematical model is adopted to describe both the multirotor and the load. After formulating the control problem, numerical validation is performed for a vehicle assumed to be a rigid body with center of gravity CG .

2.1. Reference Frames

Right-handed orthogonal reference frames are introduced according to the definitions in [32,34]:

1. an Earth-fixed north–east–down frame, $\mathcal{F}_E = \{O_E; x_E, y_E, z_E\}$: the origin, O_E , is arbitrarily fixed to a point on the Earth's surface, x_E aims in the direction of geodetic north, z_E points downward along the Earth ellipsoid normal, and y_E completes a right-handed triad. This frame is assumed to be inertial under the assumption of flat and non-rotating Earth;
2. a body-fixed frame, $\mathcal{F}_B = \{CG; x_B, y_B, z_B\}$: the longitudinal axis x_B is positive out the nose of the rotorcraft in its selected plane of symmetry, z_B aims in the direction of fuselage/frame bottom, and y_B completes a right-handed triad.
3. a rotorcraft structural reference frame, $\mathcal{F}_S = \{O_S; x_S, y_S, z_S\}$, used to locate CG and all vehicle components: axes are parallel to the body-fixed frame axes, such that $x_S = -x_B$, $y_S = y_B$, and $z_S = -z_B$. Stations (ST) are measured positive aft along the longitudinal axis. Buttlines (BL) are lateral distances, positive to the right, and waterlines (WL) are measured vertically, positive upward. Without loss of generality, it is assumed that O_S lies on the top surface of multirotor frame and is aligned vertically with multirotor geometric center over the $x_S - y_S$ plane.

A sketch of a multirotor including the selected reference frames is reported in Figure 1.

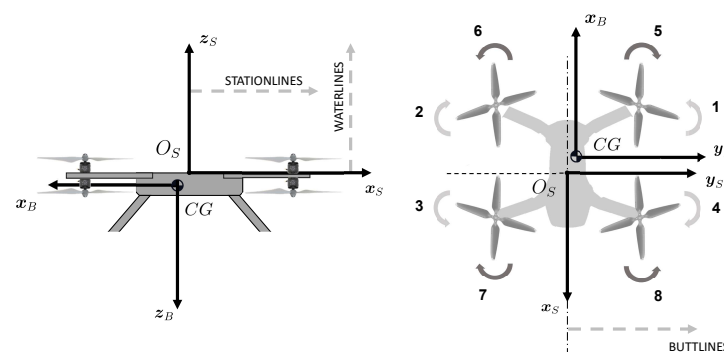


Figure 1. Multirotor body-fixed reference frames.

Vector transformation between \mathcal{F}_E and \mathcal{F}_B is provided by the rotation matrix $T_{BE}(\alpha)$ [15], obtained by a 3-2-1 Euler rotation sequence where $\alpha = [\phi, \theta, \psi]^T$ defines the attitude of the rotorcraft in terms of classical ‘roll’, ‘pitch’, and ‘yaw’ angles, respectively.

In addition to the reference frames introduced above, a third useful definition is provided for a particular Local-Vertical Local-Horizontal frame, $\mathcal{F}_H = \{CG; x_H, y_H, z_H\}$, with origin in CG. Vector transformation between \mathcal{F}_B and \mathcal{F}_H is provided by rotation matrix $T_{BH} = T_{BE}(\alpha_0)$, where $\alpha_0 = [\phi, \theta, 0]^T$ is characterized by null elementary rotation about z_E . Although the definition of \mathcal{F}_H does not provide additional information to vehicle attitude characterization, which is defined by T_{BE} , it will be useful in Section 4 for the outline of a proposed cable-swing controller.

2.2. Equations of Motion

Let $p = [p_1, p_2, p_3]^T$ be the position of multirotor and $v = [v_1, v_2, v_3]^T$ its velocity with respect to \mathcal{F}_E . The payload is assumed to be a point with mass m_l and is connected to the multirotor through a mass-less and rigid cable. The dynamics of the vehicle as expressed in \mathcal{F}_E (the subscript E will be dropped for simplicity) are described by

$$\dot{p} = v \tag{1}$$

$$m \dot{v} = f_g + f_l + f_a + f_c \tag{2}$$

where m is mass of the rotorcraft, $f_g = [0, 0, mg]^T$ is gravity force vector, f_l is the force induced by the load on the rotorcraft through the cable, and $f_a = [f_{a1}, f_{a2}, f_{a3}]^T$ is vehicle aerodynamic force, that accounts for the contributions of rotorcraft frame and rotor in-plane forces. The net thrust vector $f_c = [f_{c1}, f_{c2}, f_{c3}]^T$, directed along z_B , represents the only control input to Equation (2).

Provided the cable has constant length L , payload position with respect to the rotorcraft is uniquely identified by angles $-\pi/2 < \xi < \pi/2$ and $-\pi/2 < \zeta < \pi/2$, respectively, obtained from cable rotations about x_H - and y_H -axis (see Figure 2). In such a case, the coupled slung load dynamic model of generalized coordinate $\lambda = [p^T, \xi, \zeta]^T \in \mathbb{R}^5$ is retrieved from the work in [28], whose same nomenclature is adopted in the present framework. It is

$$\dot{\lambda} = \mu \tag{3}$$

$$M(\lambda) \dot{\mu} + C(\lambda, \mu) \mu + G(\lambda) = \tau \tag{4}$$

with $\mu = [v^T, \dot{\xi}, \dot{\zeta}]^T \in \mathbb{R}^5$ and

$$M(\lambda) = L m_l \begin{bmatrix} M/(L m_l) & 0 & 0 & 0 & c\zeta \\ 0 & M/(L m_l) & 0 & -c\zeta c\zeta & s\zeta s\zeta \\ 0 & 0 & M/(L m_l) & -s\zeta c\zeta & -c\zeta s\zeta \\ 0 & -c\zeta c\zeta & -s\zeta c\zeta & L c^2\zeta & 0 \\ c\zeta & s\zeta s\zeta & -c\zeta s\zeta & 0 & L \end{bmatrix} \tag{5}$$

$$C(\lambda, \mu) = L m_l \begin{bmatrix} 0 & 0 & 0 & 0 & -\dot{\zeta} s\zeta \\ 0 & 0 & 0 & \dot{\xi} s\zeta c\zeta + \dot{\zeta} c\zeta s\zeta & \dot{\xi} c\zeta s\zeta + \dot{\zeta} s\zeta c\zeta \\ 0 & 0 & 0 & -\dot{\xi} c\zeta c\zeta - \dot{\zeta} s\zeta s\zeta & \dot{\xi} s\zeta s\zeta - \dot{\zeta} c\zeta c\zeta \\ 0 & 0 & 0 & -L \dot{\zeta} s\zeta c\zeta & -L \dot{\xi} s\zeta c\zeta \\ 0 & 0 & 0 & L \dot{\xi} s\zeta c\zeta & 0 \end{bmatrix} \tag{6}$$

$$G(\lambda) = g L m_l [0, 0, -M/(L m_l), s\zeta c\zeta, c\zeta s\zeta]^T \tag{7}$$

provided $M = m + m_l$ is the total mass of the system. The generalized force vector τ is made of an active control contribution, τ_c , and a dissipative term, τ_a , which mostly accounts for the aerodynamic drag effects. In particular, it is $\tau_c = [f_c^T, 0, 0]^T$, while

$\tau_a = [f_a^T, 0, 0]^T - D\mu$ includes the rotorcraft aerodynamic force f_a and an additional linear damping term incorporating the effects of payload drag at low oscillation speeds, provided $D = \text{diag}(0, 0, 0, d, d)$ and $d > 0$ is a drag coefficient.

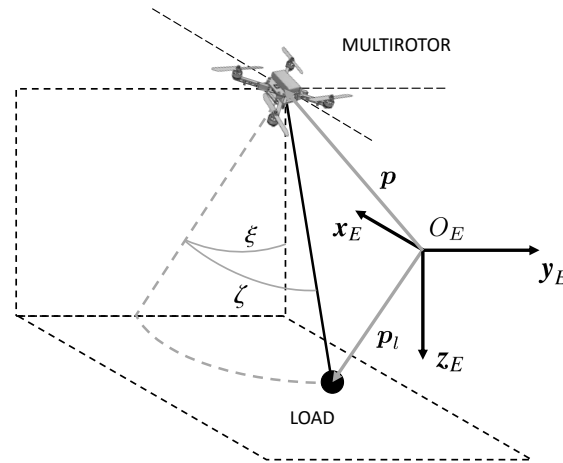


Figure 2. Definition of cable swing angles.

3. Filter Recursive Equations

Let $x = [\xi, \zeta, \dot{\xi}, \dot{\zeta}, f_{a1}, f_{a2}, f_{a3}]^T = [x_1, x_2, x_3, x_4, x_5, x_6, x_7]^T \in \mathbb{R}^7$ be the vector describing the oscillatory state of the payload and the aerodynamic disturbance affecting the rotorcraft. Define $u = f_c = [u_1, u_2, u_3]^T \in \mathbb{R}^3$ as the only input to the nonlinear system $\dot{x} = f(x, u)$, provided

$$f(x, u) = \begin{bmatrix} x_3 \\ x_4 \\ [u_2 \cos(x_1) + x_6 \cos(x_1) + u_3 \sin x_1 + x_7 \sin x_1 \\ + 2 L m x_3 x_4 \sin x_2] / [L m \cos(x_2)] \\ - [L m \cos(x_2) \sin(x_2) \xi^2 + u_1 \cos(x_2) + x_5 \cos(x_2) - u_3 \cos(x_1) \sin(x_2) \\ - x_7 \cos(x_1) \sin(x_2) + u_2 \sin(x_1) \sin(x_2) + x_6 \sin(x_1) \sin(x_2)] / (L m) \\ \mathbf{0}_{3 \times 1} \end{bmatrix} \tag{8}$$

is obtained from Equations (3)–(7), with the additional assumptions of constant or slowly varying disturbance force, namely $\dot{f}_a = \mathbf{0}_{3 \times 1}$, and null payload drag, $d = 0$. The inertially fixed acceleration of the rotorcraft is expressed as $\dot{v} = h(x, u)$, where

$$h(x, u) = \begin{bmatrix} [u_1 m + x_5 m + u_1 m_1 \cos^2(x_2) + x_5 m_1 \cos^2(x_2) + L m m_1 x_4^2 \sin(x_2) \\ - u_3 m_1 \cos(x_1) \cos(x_2) \sin(x_2) - x_7 m_1 \cos(x_1) \cos(x_2) \sin(x_2) \\ + u_2 m_1 \cos(x_2) \sin(x_1) \sin(x_2) + x_6 m_1 \cos(x_2) \sin(x_1) \sin(x_2) \\ + L m m_1 x_3^2 \cos^2(x_2) \sin(x_2)] / (m M) \\ [u_2 m + x_6 m + u_2 m_1 + x_6 m_1 - u_2 m_1 \cos^2(x_2) - x_6 m_1 \cos^2(x_2) \\ + u_2 m_1 \cos^2(x_1) \cos^2(x_2) + x_6 m_1 \cos^2(x_1) \cos^2(x_2) \\ + u_3 m_1 \cos(x_1) \cos^2(x_2) \sin(x_1) + x_7 m_1 \cos(x_1) \cos^2(x_2) \sin(x_1) \\ + u_1 m_1 \cos(x_2) \sin(x_1) \sin(x_2) + x_5 m_1 \cos(x_2) \sin(x_1) \sin(x_2) \\ - L m m_1 x_4^2 \cos(x_2) \sin(x_1) - L m m_1 x_3^2 \cos^3(x_2) \sin(x_1)] / (m M) \\ [u_3 m + x_7 m + u_3 m_1 + x_7 m_1 + g m^2 + g m m_1 \\ - u_3 m_1 \cos^2(x_1) \cos^2(x_2) - x_7 m_1 \cos^2(x_1) \cos^2(x_2) \\ + u_2 m_1 \cos(x_1) \cos^2(x_2) \sin(x_1) + x_6 m_1 \cos(x_1) \cos^2(x_2) \sin(x_1) \\ - u_1 m_1 \cos(x_1) \cos(x_2) \sin(x_2) - x_5 m_1 \cos(x_1) \cos(x_2) \sin(x_2) \\ + L m m_1 x_4^2 \cos(x_1) \cos(x_2) + L m m_1 x_3^2 \cos(x_1) \cos^3(x_2)] / (m M) \end{bmatrix} \tag{9}$$

Let $\hat{\mathbf{x}}(t)$ be the estimated state at time t obtained through the EKF predict–update dynamic model:

$$\dot{\hat{\mathbf{x}}}(t) = \mathbf{f}(\hat{\mathbf{x}}(t), \mathbf{u}(t)) + \mathbf{K}(t)(\mathbf{z}(t) - \mathbf{h}(\hat{\mathbf{x}}(t), \mathbf{u}(t))) \quad (10)$$

where $\mathbf{z}(t) = [a_1, a_2, a_3]^T \in \mathbb{R}^3$ is the vector of measured acceleration projected in \mathcal{F}_E and $\mathbf{z}(t) - \mathbf{h}(\hat{\mathbf{x}}(t), \mathbf{u}(t))$ is innovation residual. Model-based prediction is affected by multi-variate process noise $\mathbf{w}(t) \sim \mathcal{N}(0, \mathbf{Q}(t))$ with zero-mean normal distribution \mathcal{N} and covariance $\mathbf{Q}(t) \in \mathbb{R}^{7 \times 7}$. In the same way, measurement noise $\mathbf{v}(t)$ characterizes accelerometer readings with covariance matrix $\mathbf{R}(t) \in \mathbb{R}^{3 \times 3}$. Kalman gain matrix $\mathbf{K}(t) \in \mathbb{R}^{7 \times 3}$ is derived from

$$\mathbf{K}(t) = \mathbf{P}(t) \mathbf{H}^T(t) \mathbf{R}^{-1}(t) \quad (11)$$

provided that covariance estimate propagates according to

$$\dot{\mathbf{P}}(t) = \mathbf{F}(t) \mathbf{P}(t) + \mathbf{P}(t) \mathbf{F}^T(t) - \mathbf{K}(t) \mathbf{H}(t) \mathbf{P}(t) + \mathbf{Q}(t) \quad (12)$$

Unlike the discrete-time EKF, it is noted that the prediction and update steps are coupled in a continuous-time formulation [35]. From a practical standpoint, this implies that the propagation of both $\hat{\mathbf{x}}$ and \mathbf{P} must be performed by explicit or implicit numerical methods [36]. In this respect, further details are provided in the Section 4.

Finally, the state transition $\mathbf{F}(t) \in \mathbb{R}^{7 \times 7}$ and observation $\mathbf{H}(t) \in \mathbb{R}^{3 \times 7}$ matrices are respectively defined as the Jacobians:

$$\mathbf{F}(t) = \left. \frac{\partial \mathbf{f}}{\partial \mathbf{x}} \right|_{\hat{\mathbf{x}}(t), \mathbf{u}(t)}, \quad \mathbf{H}(t) = \left. \frac{\partial \mathbf{h}}{\partial \mathbf{x}} \right|_{\hat{\mathbf{x}}(t), \mathbf{u}(t)} \quad (13)$$

whose components are listed in Appendix A.

Remark 1. Input $\mathbf{u}(t)$ in Equation (10) is assumed to be known. As a matter of fact, the exact knowledge of control force is not directly available in practical applications, where detailed models of powerplant subsystems and propellers aerodynamics would be required. In what follows, a sample solution is proposed for multirotor vehicles to address model uncertainty through measurements without the need for ad hoc devices or accurate characterization of propulsion units. Based on the definition in Section 2.2, the control force is expressed as $\mathbf{f}_c = -T \mathbf{z}_B = \mathbf{T}_{BE}^T [0, 0, -T]^T$, where T is net thrust generated by rotors along \mathbf{z}_B . Taking into account Equation (2), the estimated thrust magnitude \hat{T} can be calculated according to

$$\hat{T} = \left\| m \mathbf{z} - \hat{\mathbf{f}}_g - \hat{\mathbf{f}}_l - \hat{\mathbf{x}}_{5:7} \right\| \quad (14)$$

where $\|\cdot\|$ is Euclidean norm, $\hat{\mathbf{f}}_g = [0, 0, m \hat{g}]^T$, \hat{g} is measured gravity acceleration, and $\hat{\mathbf{f}}_l = [0, 0, m_l \hat{g}]^T$ is the force induced by the load on the rotorcraft under the assumption that the cable is exactly directed along the local vertical, as it occurs in near-hovering equilibrium condition. Finally, $\hat{\mathbf{x}}_{5:7} = [\hat{x}_5, \hat{x}_6, \hat{x}_7]^T$ is the vector of filter-estimated aerodynamic force, that includes external disturbances and rotor forces over the $\mathbf{x}_B - \mathbf{y}_B$ plane. Reconstructed input for filtering purposes is thus obtained as $\hat{\mathbf{u}} = \hat{\mathbf{T}}_{BE}^T [0, 0, -\hat{T}]^T$, provided $\hat{\mathbf{T}}_{BE}$ is the rotation matrix calculated from measured attitude information. Extension of the proposed method to conventional helicopter configurations can be conceived with minimum effort by accounting both tail rotor and main rotor contributions for the estimation of net control force.

4. Results

Filter validation is performed by numerical simulations and an experimental campaign. In the first case, a cargo octarotor is shown to perform sample delivery maneuvers of a relatively large payload with and without the activation of a basic swing-damping controller.

In the second case, the approach is addressed for a small-scale quadrotor application, provided the estimated swing state is compared to direct measurements obtained through potentiometer readings.

4.1. Simulation Results

4.1.1. Simulation Setup

Simulations are performed in a Matlab® environment with a fourth-order Runge–Kutta solver frequency of 500 Hz [36]. The octarotor is modeled as a rigid body, while the payload is assumed to be a point mass attached through a linear-elastic cable to a hook point H , distinct from the rotorcraft center of gravity CG . The modeling follows the same approach and nomenclature adopted in [15], while relevant system parameters are listed in Table 1. The payload is affected by aerodynamic drag, provided $A_l = \pi R_l^2$ is the frontal area of an equivalent sphere with radius $R_l = 0.5$ m and drag coefficient $C_{dl} = 0.5$. An octarotor platform is considered, characterized by a set of eight contra-rotating propellers (see Figure 1). The cross-shaped planar configuration is characterized by $STA_{R_1} = STA_{R_2} = STA_{R_5} = STA_{R_6} = -STA_{R_3} = -STA_{R_4} = -STA_{R_7} = -STA_{R_8} = -0.690$ m, $BL_{R_1} = BL_{R_4} = BL_{R_5} = BL_{R_8} = -BL_{R_2} = -BL_{R_3} = -BL_{R_6} = -BL_{R_7} = 0.690$ m, $WL_{R_1} = WL_{R_2} = WL_{R_3} = WL_{R_4} = -0.024$ m, and $WL_{R_5} = WL_{R_6} = WL_{R_7} = WL_{R_8} = -0.238$ m.

Table 1. Multirotor slung load system parameters.

Parameter	Symbol	Value	Units
Multirotor			
Mass	m	70	kg
Center of gravity position	$STA_{CG} = BL_{CG}$	0	m
	WL_{CG}	−0.15	m
Moments of inertia	J_{11}	10.61	kg m ²
	J_{22}	10.31	kg m ²
	J_{33}	19.74	kg m ²
	J_{12}	0.037	kg m ²
	J_{13}	−0.043	kg m ²
	J_{23}	−0.003	kg m ²
Center of pressure position	$STA_{CP} = BL_{CP}$	0	m
	WL_{CP}	−0.125	m
Frame drag areas	$A_1 = A_2$	0.22	m ²
	A_3	1.03	m ²
Propeller			
Number of blades	n_b	2	
Radius	R	0.5	m
Mean aerodynamic chord	\bar{c}	0.086	m
Chord @ 75% R	c_{75}	0.103	m
Lift curve slope	a	5.9	rad ^{−1}
Pre-cone angle	a_0	0	rad
Root pitch angle	θ_0	0.7854	rad
Total twist	θ_t	−0.6981	rad
Load			
Mass	m_l	100	kg
Reference area	A_l	0.785	m ²
Drag coefficient (sphere)	C_{dl}	0.5	
Cable			
Nominal cable length	L	15	m
Hooke’s constant	K	90,950	N/m
Hook point position	$STA_H = BL_H$	0	m
	WL_H	−0.3	m

Rotor forces and moments are calculated by means of Blade Element Momentum Theory. With respect to the thrust and torque contributions only, a simplified model is proposed as in [15], such that

$$T_j = k_T \Omega_j^2, \quad Q_j = k_Q \Omega_j^2 \tag{15}$$

where $k_T = \gamma \bar{k}_T$ and $k_Q = \gamma \bar{k}_Q$. \bar{k}_T and \bar{k}_Q are positive constants determined experimentally at air density $\bar{\rho}$, while $\gamma = \rho/\bar{\rho}$ is a density scaling parameter. In the present case, upper rotors (1–4) are characterized by $\bar{k}_T|_{up} = 2.90 \cdot 10^{-3} \text{ N}/(\text{rad/s})^2$, while lower rotors (5–8) present $\bar{k}_T|_{down} = 2.20 \cdot 10^{-3} \text{ N}/(\text{rad/s})^2$, accounting for reduced efficiency due to wake interaction with upper rotors [37]. Finally, $\bar{k}_Q = 1.25 \cdot 10^{-4} \text{ Nm}/(\text{rad/s})^2$ at the reference density $\bar{\rho} = 1.1229 \text{ kg/m}^3$. The characterization of rotor induced speed is performed by assuming a uniform inflow field. The computation is performed through the static model proposed in [32], which is numerically solved according to *fzero* Matlab[®] routine by Dekker with initial condition for the induced speed equal to -10 m/s [38]. Air parameters are calculated from the International Standard Atmosphere (ISA) model as a function of altitude [39].

Although modern control approaches and technologies can be conceived to track a desired condition in complex scenarios [40], it is here assumed that guidance, navigation, and control tasks are performed, without loss of generality, through a programmable standard based on Pixhawk board (which integrates necessary sensors and algorithms for state estimation). In this respect, a cascaded controller shaped on PX4 architecture and notation [41] is considered to stabilize the octarotor according to different flight modes, from high-level position control to direct attitude regulation (see Figure 3). Provided a detailed analysis of PX4 control functions is out of the scope of the present paper, it is supposed that stabilization of the isolated vehicle is performed according to prescribed flying qualities through a dedicated tuning of control parameters. The dynamics of the single electric propulsion unit made of Electronic Speed Controller (ESC) and brushless motor are modeled by a first-order transfer function with time constant $\tau_{em} = 0.06 \text{ s}$, accounting for both electric and mechanical non-ideal effects. The transfer function transforms the desired value of angular rate into the actual value generated by the motor shaft.

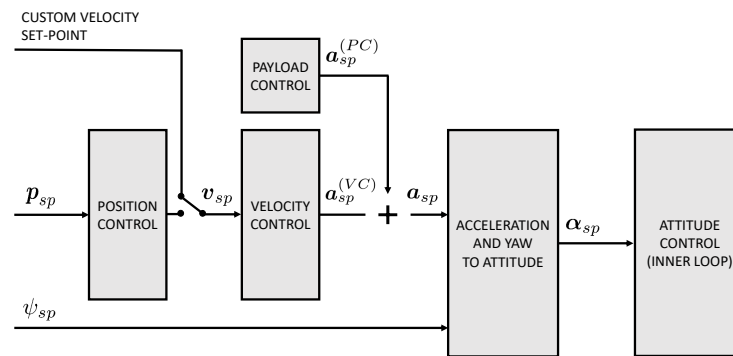


Figure 3. Multirotor and payload control scheme based on PX4 autopilot architecture [41].

Onboard computer is located in $STA_{PIX} = BL_{PIX} = 0 \text{ m}$ and $WL_{PIX} = -0.1 \text{ m}$, with axes aligned with \mathcal{F}_B axes. To simulate the effects of sensor noise, zero-mean Gaussian white noise is added to each Euler angle and angular velocity measurement, with standard deviations $\sigma_\alpha = 0.5 \text{ deg}$ and $\sigma_\omega = 0.1 \text{ deg/s}$, respectively. The body-fixed accelerometer readings are obtained by adding white Gaussian noise with $\sigma_{acc} = 0.0057 \text{ m/s}^2$ and a constant bias vector $\mathbf{b}_{acc} = [0.015, -0.01, 0.002]^T \text{ m/s}^2$ to the simulated values. Estimation error noise is also considered for vehicle position and velocity expressed in \mathcal{F}_E , where standard deviations $\sigma_p|_{xy} = 0.074 \text{ m}$ and $\sigma_v|_{xy} = 0.057 \text{ m/s}$ affect motion over the local-horizontal plane, while $\sigma_p|_z = 0.034 \text{ m}$ and $\sigma_v|_z = 0.036 \text{ m/s}$ characterize the vertical

channel. Sampling is performed by a frequency of 250 Hz (sample time $\Delta t = 0.004$ s), the same adopted for the generation of control signals and the state-estimation routine, which includes the integration of Equations (10) and (12) through a fourth-order Runge–Kutta solver [36].

Filter initial state is set to $\hat{x}_0 = \mathbf{0}_{7 \times 1}$ and the estimated covariance matrix is initialized with $\mathbf{P}_0 = \text{diag}(10^{-6}, 10^{-6}, 10^{-6}, 10^{-6}, 2, 2, 10^{-5})$. Let \mathbf{I}_m be the unit matrix with dimension m . The assigned noise covariance matrix is $\mathbf{R} = 3.6 \cdot 10^{-5} \cdot \mathbf{I}_3 \text{ m}^2/\text{s}^4$ and process noise is accounted by $\mathbf{Q} = \text{diag}(10^{-7}, 10^{-7}, 10^{-7}, 10^{-7}, 1, 1, 10^{-7})$, both matrices assumed to be constant. Uncertainties on relevant filter parameters are also considered. In particular, the assumed payload mass is $\hat{m}_l = 0.9 \cdot m_l = 90$ kg, with -10% error.

In order to minimize cable swing angles and rates, an auxiliary payload controller (PC) is proposed to generate a set-point acceleration vector $\mathbf{a}_{sp}^{(PC)}$ with components expressed in \mathcal{F}_E . Such acceleration is added to the contribution $\mathbf{a}_{sp}^{(VC)}$ determined by the velocity controller (VC) in Figure 3. With the aim to (1) generate the auxiliary control action or (2) to compare filter-estimated variables with potentiometer readings during experiments, swing angles and rates are conveniently estimated with respect to the local frame \mathcal{F}_H , which is obtained if \mathbf{z} and \mathbf{u} are projected in \mathcal{F}_H (it is noted that, if ψ is a constant or a slowly varying attitude parameter, \mathcal{F}_H can be assumed to be an inertial frame). The auxiliary controller, based on a heuristic approach, assumes the form:

$$\mathbf{a}_{sp}^{(PC)} = \mathbf{T}_{EH} \left(\begin{bmatrix} k_{D\zeta} & 0 & 0 \\ 0 & k_{D\dot{\zeta}} & 0 \\ 0 & 0 & 0 \end{bmatrix} \begin{bmatrix} \dot{\zeta}_H \\ \dot{\zeta}_H \\ 0 \end{bmatrix} + \begin{bmatrix} k_{P\zeta} & 0 & 0 \\ 0 & k_{P\dot{\zeta}} & 0 \\ 0 & 0 & 0 \end{bmatrix} \begin{bmatrix} \zeta_H \\ \zeta_H \\ 0 \end{bmatrix} \right) \quad (16)$$

where $\mathbf{T}_{EH} = \mathbf{T}_{BH}^T \mathbf{T}_{BE}^T$ accounts for vector transformation between \mathcal{F}_H and \mathcal{F}_E and is defined by an elementary rotation about \mathbf{z}_H with amplitude ψ . Control gains are positive with values $k_{D\dot{\zeta}} = k_{D\zeta} = 2 \text{ m}/(\text{rad s})$ and $k_{P\dot{\zeta}} = k_{P\zeta} = 9 \text{ m}/(\text{rad s}^2)$.

4.1.2. Preliminary Definitions

Indicators are preliminarily defined with the aim to characterize the performance of simulation cases. The effect of payload active stabilization will be thus investigated and performance indices will assess the validity of the approach for each proposed maneuver. Five different indicators are introduced:

- Maneuver time, t_m . It is the total time required to conclude the considered maneuver, based on a stop criterion. In the present framework, the simulation is stopped when two conditions are met, namely: (1) the positioning error $\varepsilon = \|\mathbf{p}_{sp} - \mathbf{p}\|$ falls below 0.1 m and (2) cable oscillation angle $\chi \geq 0$ remains bounded below 1 deg for a prescribed time of 10 s. In the case when the considered maneuver does not require position stabilization, t_m is calculated on the basis of condition 2 only. Cable oscillation angle χ is defined as the angle between the local vertical axis and the direction of the cable. Considering the nomenclature adopted in [15], χ is obtained from the dot product:

$$\chi = \arccos(\mathbf{z}_H \cdot \hat{\mathbf{c}}) \quad (17)$$

where $\hat{\mathbf{c}} = \mathbf{c}/\|\mathbf{c}\|$ is the unit vector directed from the suspension point to the payload.

- Average swing angle, $\bar{\chi}$. It is calculated through the integral

$$\bar{\chi} = \frac{1}{t_m} \int_0^{t_m} \chi(s) ds \quad (18)$$

over maneuver time domain. Although $\bar{\chi}$ correctly describes the overall oscillation behavior on average, the integral quantity $\bar{\chi} \cdot t_m = \int_0^{t_m} \chi(s) ds$ is also accounted to provide an indication of how much and how long the cable remains far from the vertical equilibrium condition.

- Average swing rate, \bar{v} . Let $v = \dot{\chi}$ be the swing rate, defined as the time derivative of $\chi(t)$. Then, \bar{v} is calculated through the integral

$$\bar{v} = \sqrt{\frac{1}{t_m} \int_0^{t_m} v^2(s) ds} \tag{19}$$

Similar to the case of $\bar{\chi}$, the integral quantity $\sqrt{\int_0^{t_m} v^2(s) ds}$ is also determined to provide a better indication of how much and how long the swing rate remains far from the equilibrium null condition.

- Average trajectory-tracking error, \bar{d} . It is calculated as the integral

$$\bar{d} = \frac{1}{t_m} \int_0^{t_m} d(s) ds \tag{20}$$

of the time-dependent variable $d(t) \geq 0$. In the present case, $d(t)$ describes the accuracy of point-to-point positioning maneuvers in the framework of waypoint navigation. Assume A and B are consecutive waypoints, respectively, identified by position vectors \mathbf{p}_A and \mathbf{p}_B . $d(t)$ represents the distance at time t of the vehicle from the direction defined by vector $\mathbf{p}_B - \mathbf{p}_A$, calculated over the local-horizontal plane $\mathbf{x}_E - \mathbf{y}_E$.

- Total propulsive energy, E_{prop} . It is the mechanical energy delivered by electrical motors to propellers, evaluated from the integral

$$E_{prop} = \int_0^{t_m} \sum_{i=1}^8 P_{shi}(s) ds \tag{21}$$

where $P_{shi} = Q_i \Omega_i$ is the output shaft power generated by the i -th motor, obtained from required torque Q_i and angular rate Ω_i under the assumption of null friction torque.

4.1.3. Filter Validation

Different test cases are analyzed to validate both the estimation and the control strategies.

In the first case ('1'), the octarotor starts from a hovering condition at $\mathbf{p}(0) = [0, 0, -30]^T$ m with $\zeta(0) = \zeta(0) = 20$ deg and $\dot{\zeta}(0) = \dot{\zeta}(0) = 0$ deg/s and is required to keep the initial position in the absence of wind ($\mathbf{p}_{sp} = \mathbf{p}(0)$). Stabilization of vehicle position, initially perturbed by payload non-null conditions, occurs with $\mathbf{a}_{sp}^{(PC)} = \mathbf{0}_{3 \times 1}$ as in Figure 4, where positioning error $\mathbf{e}_p = \mathbf{p}_{sp} - \mathbf{p} = [e_{p1}, e_{p2}, e_{p3}]^T$ components are plotted over time.

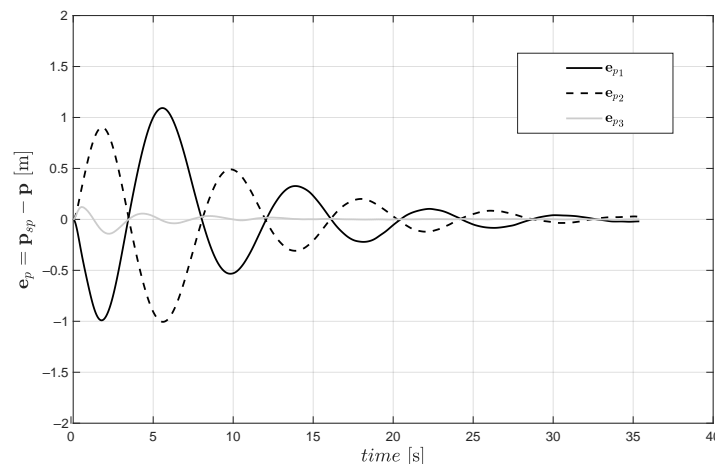


Figure 4. Stabilization of octarotor positioning error (Case 1, no active payload stabilization).

Cable oscillations slowly decay under dissipative effects related to both vehicle speed stabilization and aerodynamic drag affecting the payload, provided maneuver time is $t_m = 35.4$ s. With respect to filter performance, a comparison between the true and the estimated angle and rate is reported in Figure 5, showing convergence of the algorithm.

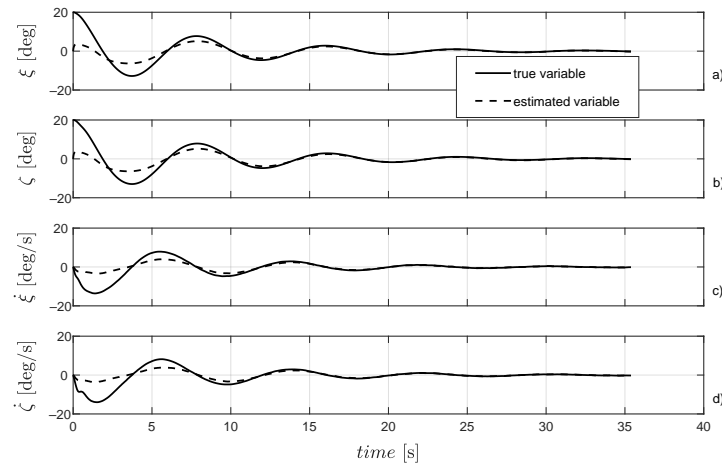


Figure 5. Comparison between the true and the estimated oscillation variables (Case 1, no active payload stabilization).

Assume the auxiliary payload controller is activated with control gains given above. Figure 6 shows the effectiveness of the approach based on the feedback of estimated variables, such that maneuver time is reduced to $t_m = 23.9$ s and oscillation variables are rapidly damped. Cable swing angle χ reaches and remains below 5% of the initial value in only 13.5 s, provided the same condition is obtained in about 24.6 s when active payload stabilization does not provide contribution.

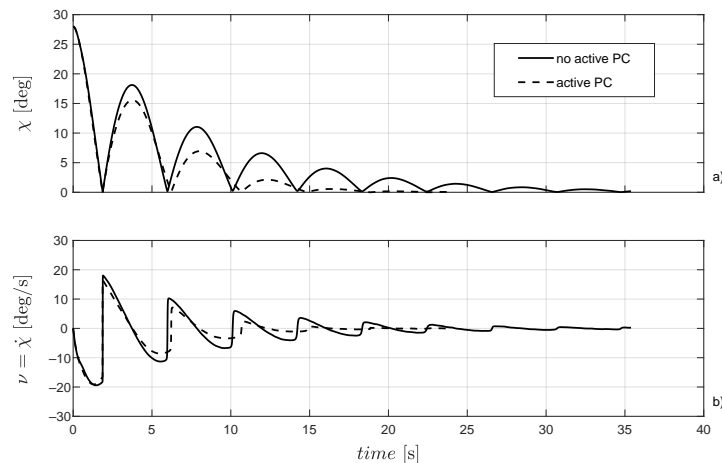


Figure 6. Stabilization of oscillation angle χ and rate ν with and without the activation of payload controller (Case 1).

With respect to other performance indicators, Table 2 summarizes the main results and computes percentage errors. Note that the proposed maneuver is representative of a conservative test case, provided the filter is initialized with zero state estimate in the presence of non-zero real state. Such a condition is not encountered in practice and shows in full the phase before filter stabilization (thus affecting closed-loop performance). The activation of PC determines a strong reduction in the mechanical energy required to conclude the maneuver, which is determined by the faster decay of oscillation variables. Moreover, if one considers the quantity $\bar{\chi} \cdot t_m$, which is the integral of oscillation angle

over maneuver time t_m , a reduction of $\bar{\chi}$ -33.2% is obtained. The same considerations hold for the integral quantity $\sqrt{\int_0^{t_m} v^2(s) ds}$, for which a reduction of -13.7% is calculated.

Table 2. Case 1: summary of performance indicators.

Index	No Active PC	Active PC	Error [%]
t_m [s]	35.4	23.9	-32.6
$\bar{\chi}$ [deg]	4.20	4.16	-1
\bar{v} [deg/s]	5.53	5.82	$+5.2$
\bar{d} [m]	0.33	0.63	$+90.9$
E_{prop} [kJ]	820.7	553.9	-32.5

It is noteworthy that improved performance in terms of payload stabilization comes at the cost of increased \bar{d} index ($+90.9\%$). From a physical standpoint, this was to be expected: since the overall system is underactuated, both the positioning and the payload control tasks are performed by making the octarotor simultaneously track the desired accelerations $a_{sp}^{(VC)}$ and $a_{sp}^{(PC)}$. The latter contribution is intentionally designed to force the controlled system to exhibit two-time-scale behavior as in [14], fast for the oscillation dynamics and slow for the velocity-tracking task. While determining time-scale separation, $a_{sp}^{(PC)}$ perturbs $a_{sp}^{(VC)}$ as in Figure 7, where the sign of the dot product $a_{sp}^{(VC)} \cdot a_{sp}^{(PC)}$ is reported as a function of time, showing partial vector opposition in the very first part of the maneuver (when $t \leq 6$ s). During such a phase, d reaches higher values and then rapidly decreases while taking benefits of fast payload stabilization.

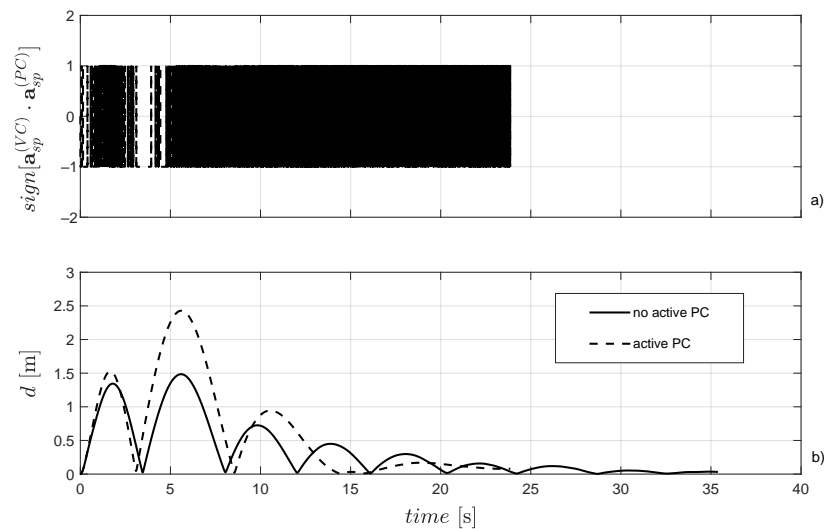


Figure 7. (a) Analysis of desired acceleration vector contributions; (b) stabilization of error distance d with and without the activation of dedicated payload controller (Case 1).

In the second case ('2'), the octarotor is requested to leave the initial hovering condition with $\zeta(0) = \dot{\zeta}(0) = 0$ deg and $\dot{\zeta}(0) = \ddot{\zeta}(0) = 0$ deg/s and track the set-point velocity $v_{sp} = [5, 0, 0]^T$ m/s for $t < 30$ s and $v_{sp} = [0, 0, 0]^T$ m/s for $t \geq 30$ s, with components expressed in \mathcal{F}_E . A horizontal north wind with constant 1 m/s intensity is assumed to oppose rotorcraft motion.

Performance indicators are summarized in Table 3, showing the beneficial effect of $a_{sp}^{(PC)}$. If one considers $\bar{\chi} \cdot t_m$, a reduction of -51.1% is obtained, while the integral quantity $\sqrt{\int_0^{t_m} v^2(s) ds}$ is reduced by -34.4% . Stabilization of octarotor speed is depicted in Figure 8, where $e_v = v_{sp} - v = [e_{v1}, e_{v2}, e_{v3}]^T$ is plotted over time with components

in \mathcal{F}_E . A comparison between the true and the estimated ζ angle and rate is reported in Figure 9.

Table 3. Case 2: summary of performance indicators.

Index	No Active PC	Active PC	Error [%]
t_m [s]	66.9	49.0	−26.8
$\bar{\chi}$ [deg]	3.99	2.66	−33.3
\bar{v} [deg/s]	5.04	3.86	−23.4
\bar{d} [m]	N/A	N/A	N/A
E_{prop} [kJ]	1553.1	1136.5	−26.8

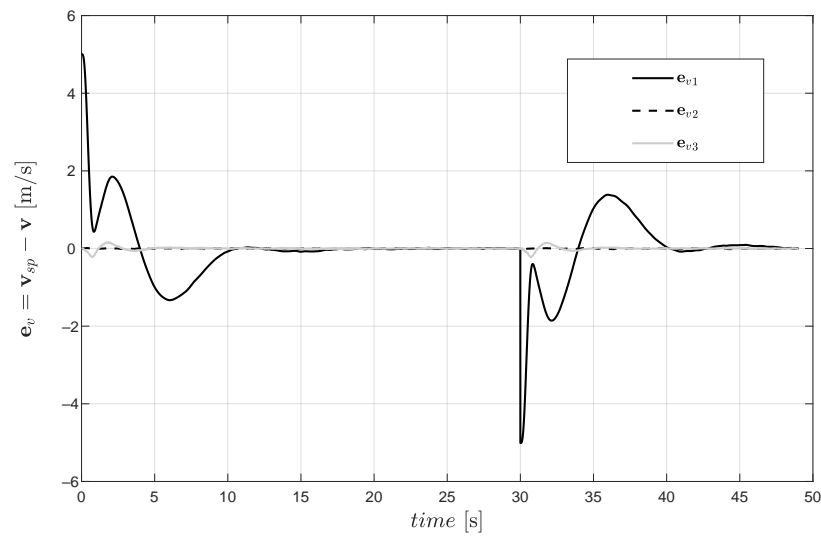


Figure 8. Stabilization of octarotor velocity error (Case 2, active payload stabilization).

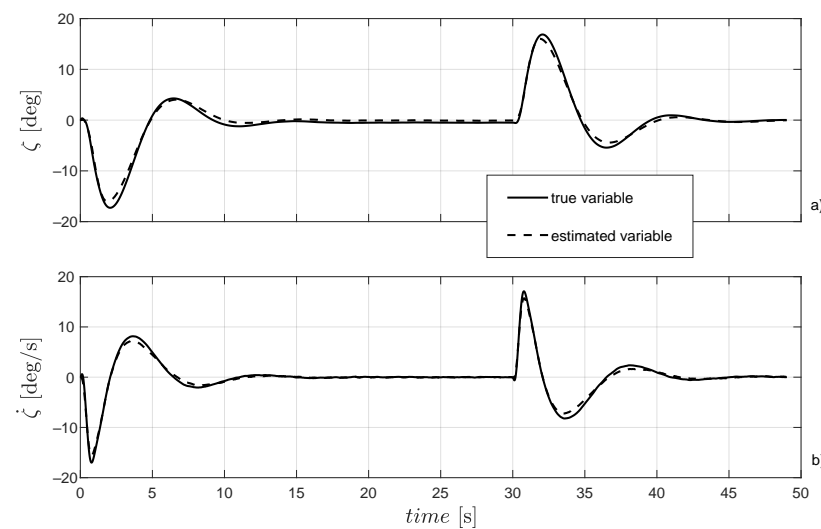


Figure 9. Comparison between the true and the estimated variables ζ and $\dot{\zeta}$ (Case 2, active payload stabilization).

The estimation of disturbance force $\hat{f}_a = \hat{x}_{5:7}$ represents a fundamental task in the present case, where performance of forward flight in the presence of wind is significantly affected by octarotor frame drag and rotor in-plane forces. In Figure 10, estimated disturbance forces are compared to exact variables. It can be noted how EKF is able to track the force components with satisfactory accuracy after the required transients where both

vehicle speed and EKF outputs oscillate prior to stabilization. A residual estimation error characterizes the steady-state response of the algorithm (for example, the estimated f_{a2} component sets on a constant value equal to -1.3 N, different from the expected zero value, as obtained by averaging filter output between 20 s and 30 s). Such a behavior is traceable to the uncertainty in the knowledge of payload mass and the presence of accelerometer bias.

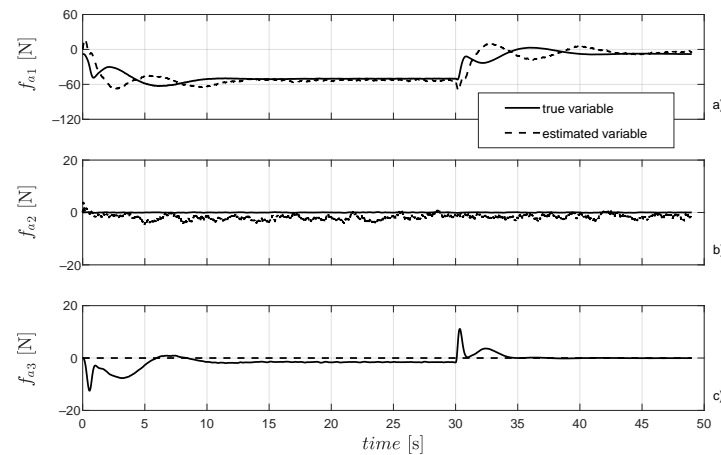


Figure 10. Comparison between the true and the estimated disturbance forces (Case 2, active payload stabilization).

Both non-ideal effects influence algorithm performance in two ways: (1) directly, through EKF equations detailed in Appendix A, and (2) indirectly, through input reconstruction as described in Remark 1, where system data and measurement z are used to estimate the generated thrust amplitude. However, it must be pointed out that the considered simulation setup comes under a conservative approach. First, most commercial off-the-shelf devices, such as Pixhawk platform, already include bias-compensation routines. With respect to the uncertainty on the knowledge of payload or cable parameters, it is recommended to update the filter setup according to the particular flight configuration, provided payload data are preliminarily measured or (possibly) online-estimated [42]. It is the case, for example, when the movement of goods is performed in large storehouses, where scheduling of system parameters, filter covariance matrix Q , and control gains can be modified according to the particular object to relocate. On the other hand, when payload mass is uncertain and cannot be estimated with sufficient accuracy, automated filter tuning techniques can be envisaged, provided that the adaptation of Q is adopted for (at least partial) mitigation of model uncertainties [43].

In the third case ('3'), the octarotor starts from the same condition of Case 2; it is requested to track a set of prescribed waypoints WP_i , $i = 1, \dots, 7$ (see Table 4) and perform a return-to-home maneuver. Each target waypoint is assumed to be reached when its distance from the vehicle decreases below 1.5 m. The first line of Table 4), relative to the first waypoint, coincides with the initial octarotor position.

Table 4. Case 3: waypoint list (components expressed in \mathcal{F}_E).

i -th Waypoint	x_i [m]	y_i [m]	z_i [m]
1	0	0	-30
2	10	0	-50
3	20	-10	-50
4	20	10	-50
5	30	0	-50
6	10	0	-50
7	0	0	-30

During the mission, gusts are generated to perturb the state of both the octarotor and the payload. The adopted turbulence model, implemented by a dedicate block available from Simulink Aerospace Blockset, adopts the Von Kármán spectral representation to add turbulence by passing band-limited white noise through appropriate forming filters. In particular, the block treats the linear and angular velocity components of continuous gusts as spatially varying stochastic processes and specifies each component's power spectral density [44]. The approach is based on the mathematical representation in the Military Specification MIL-F-8785C and Military Handbook MIL-HDBK-1797B, respectively, provided in [45,46]. The following parameters are set:

- specification: MIL-F-8785C;
- model type: continuous Von Kármán (+q +r);
- wind speed at 6 m (used to define the low-altitude wind intensity): 10 m/s;
- wind direction at 6 m (degrees clockwise from north): 90 deg;
- scale length at medium/high altitudes: 533.4 m (default value);
- band-limited noise sample time: 0.002 s;
- MR wingspan: 2.38 m (here intended as the maximum octarotor frontal size);
- load wingspan: 1 m (here intended as the maximum load frontal size).

It is noted that the Simulink-based Von Kármán model is well defined for fixed-wing aircraft, for which non-null speed conditions are expected in flight. This is not the case of rotary-wing platforms, where the possibility to perform hovering flight makes the wind model not suitable for application. A conservative approach is, however, adopted, where required input speed to the model is calculated as the sum of octarotor actual speed and the maximum desired speed (10 m/s) that the position autopilot of PX4 algorithm is allowed to generate. In addition to the considered turbulence contribution, a horizontal north wind with constant 8 m/s intensity is considered. By taking into account such severe atmospheric conditions, the termination criterion in Section 4.1.2 is conveniently relaxed. In particular, the maneuver is assumed to be concluded when (1) positioning error ε with respect to the last waypoint falls below 0.5 m and (2) cable oscillation angle χ remains bounded below 5 degrees for a prescribed time of 10 s.

In Figure 11, the trajectory followed by the octarotor is reported for the case when $\mathbf{a}_{sp}^{(PC)} = \mathbf{0}_{3 \times 1}$. Figure 12 depicts wind contributions in terms of linear velocities and angular rates, with components projected in \mathcal{F}_E . The obtained performance indicators are reported in the second column of Table 5.

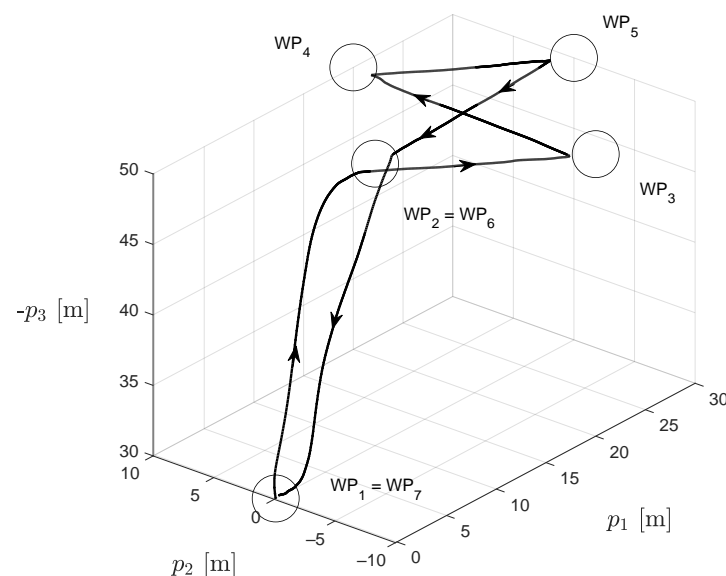


Figure 11. Trajectory followed by the octarotor based on a set of prescribed waypoints WP_i , $i = 1, \dots, 7$ (Case 3, no active payload stabilization).

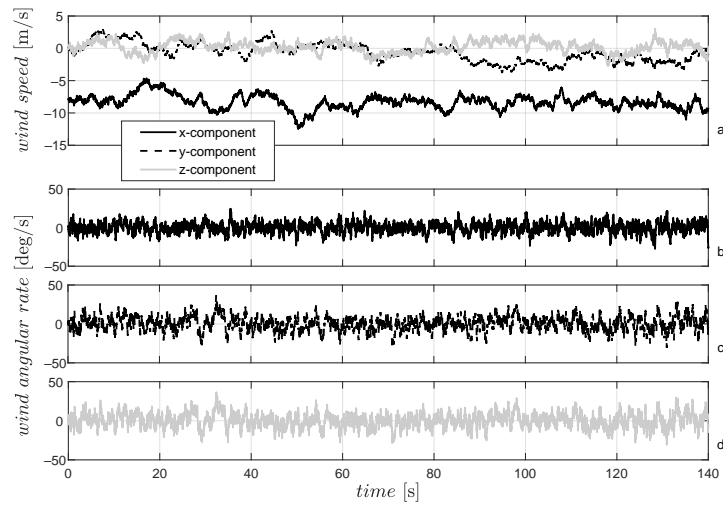


Figure 12. Wind speed and angular rate components projected in \mathcal{F}_E (Case 3, no active payload stabilization).

Assume that PC is activated based on the closed-loop feedback of EKF-estimated variables. The third column of Table 5 summarizes the main results and computes percentage errors with respect to the case when no active PC is adopted. As expected, no significant difference characterizes the comparison in terms of both maneuver time and energy, provided that waypoint transition is performed only on the basis of positioning error, with no particular requirement on residual cable swing angle (except for the final waypoint). It is a fact, however, that $\bar{\chi}$ and \bar{v} are, respectively, reduced by 23% and 34.9%, showing improved behavior of swing condition with comparable trajectory-tracking parameter performance, \bar{d} (−0.2%).

Table 5. Case 3: summary of performance indicators.

Index	No Active PC	Active PC (EKF)	Active PC (FGDF)
t_m [s]	140.3	139.8 (−0.4%)	140.3 (+0%)
$\bar{\chi}$ [deg]	2.22	1.71 (−23.0%)	1.77 (−20.3%)
\bar{v} [deg/s]	1.86	1.21 (−34.9%)	1.27 (−31.7%)
\bar{d} [m]	6.49	6.48 (−0.2%)	6.52 (+0.5%)
E_{prop} [kJ]	3242.5	3230.1 (−0.4%)	3249.9 (+0.2%)

The proposed approach, based on a nonlinear extended-state estimator, is further validated in Case 3 with respect to the FGDF solution provided in [28], whose same nomenclature and definitions are adopted. In such a framework, the reduced-order swing state $\mathbf{x}^{FGDF} = [\xi, \zeta, \dot{\xi}, \dot{\zeta}]^T \in \mathbb{R}^4$ approximately evolves according to $\dot{\mathbf{x}}^{(FGDF)} = \mathbf{A} \mathbf{x}^{(FGDF)} + \mathbf{B} \mathbf{u}^{FGDF}$, which are system dynamics obtained from linearization of Equations (10)–(14) in [28] about the hovering condition. $\mathbf{u}^{FGDF} \in \mathbb{R}^2$ accounts for the first two components of \mathbf{u} , expressed in \mathcal{F}_H . By accounting for the same model uncertainties described above, matrices \mathbf{A} and \mathbf{B} result to be, respectively:

$$\mathbf{A} = \begin{bmatrix} 0 & 0 & 1 & 0 \\ 0 & 0 & 0 & 1 \\ -1.4943 & 0 & 0 & 0 \\ 0 & -1.4943 & 0 & 0 \end{bmatrix}, \quad \mathbf{B} = 10^{-4} \cdot \begin{bmatrix} 0 & 0 \\ 0 & 0 \\ 0 & 9.524 \\ -9.524 & 0 \end{bmatrix} \quad (22)$$

In terms of difference equations, the true state vector $\mathbf{x}_k^{(FGDF)}$ at time k propagates according to $\mathbf{x}_{k+1}^{(FGDF)} = \Phi_k \mathbf{x}_k^{(FGDF)} + \Gamma_k \mathbf{u}_k^{(FGDF)}$. The state-transition matrix for the estima-

tion algorithm is obtained as $\Phi_k = \Phi = \exp(A \Delta t)$ and implemented by means of Matlab[®] matrix exponential function $\text{expm}(\cdot)$, according to the method in [47]:

$$\Phi = \begin{bmatrix} 1 & 0 & 0.004 & 0 \\ 0 & 1 & 0 & 0.004 \\ -0.006 & 0 & 1 & 0 \\ 0 & -0.006 & 0 & 1 \end{bmatrix} \tag{23}$$

The control-input model is calculated as $\Gamma_k = \Gamma = A^{-1}(\Phi - I_m) B$, namely:

$$\Gamma = 10^{-6} \cdot \begin{bmatrix} 0 & 0.008 \\ -0.0088 & 0 \\ 0 & 3.81 \\ -3.81 & 0 \end{bmatrix} \tag{24}$$

The observation $z_k^{(FGDF)} = [\zeta_{syn}, \zeta_{syn}]_k^T \in \mathbb{R}^2$, derived from simple acceleration information as in [28], approximately tracks the dynamic process as in $z_k^{(FGDF)} = H^{(FGDF)} x_k^{(FGDF)}$, where

$$H^{(FGDF)} = \begin{bmatrix} 1 & 0 & 0 & 0 \\ 0 & 1 & 0 & 0 \end{bmatrix} \tag{25}$$

is the observation matrix. Synthetic angle measurements in $z_k^{(FGDF)}$ are corrupted by noise $v_k^{(FGDF)} \in \mathbb{R}^2$ with variance $R^{(FGDF)}$, namely $z_k^{(FGDF)} = H^{(FGDF)} x_k^{(FGDF)} + v_k^{(FGDF)}$. In the present case, it is $R^{(FGDF)} = 2.465 \cdot 10^{-4} \cdot I_2 \text{ rad}^2$.

For the sake of brevity, the tuning and scaling procedure described in [28] to find the globally optimum FGDF configuration is not reported. The final results are directly provided, where $\beta = \beta_T = 0.998$ represents the best fading factor at which the estimated measurement noise covariance matrix $\hat{R}^{(FGDF)}$ satisfies $\hat{R}^{(FGDF)} \approx R^{(FGDF)}$. EKF and FGDF algorithms are switched on in parallel during the maneuver of Case 3, while no active payload stabilization is performed. FGDF is initialized with null state vector and nominal error covariance $(E^-)_0^{(FGDF)} = 10^{-7} \cdot I_4$.

Figures 13–16 depict the output of the two filters in terms of swing angles and rates. Plot details are also reported to highlight the differences between the results of estimation methods. Improved performance characterizes EKF for all considered variables, especially when high oscillation angles and rates occur (see, for example, what happens during the time interval $40 \leq t \leq 60$ s, when position controller drives the vehicle from WP_3 to WP_4 and excites lateral payload oscillations) or when near-hover flight in the presence of wind is performed. The latter case shows up during time interval $120 \leq t \leq 130$ s, when the octarotor is required to keep the position represented by WP_7 with non-null attitude to counteract the steady wind contribution. During this terminal flight phase, an evident estimation bias characterizes the output of the linear algorithm. It is noteworthy that the estimation bias of FGDF particularly affects the frontal angle ζ and rate $\dot{\zeta}$, as in Figures 15 and 16. Such a behavior is determined by the presence of a dominant wind contribution from the north that induces disturbance forces on both the vehicle and the suspended load. For the sake of completeness, it is pointed out that estimation error on ζ also characterizes the EKF output (although to a lesser extent). Such a drawback comes after neglecting payload drag in both the estimation methods, thus introducing model uncertainty. However, overall EKF performance remains satisfactory and proves to be preferable to that obtained in the linear framework.

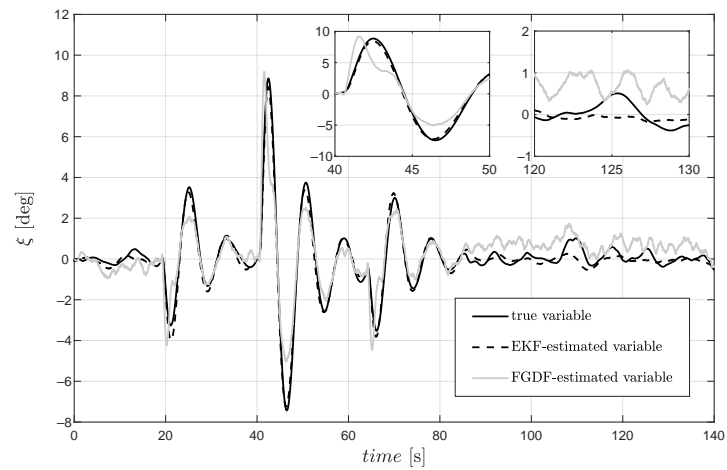


Figure 13. Comparison between the true and the estimated swing angle ζ (Case 3, no active payload stabilization).

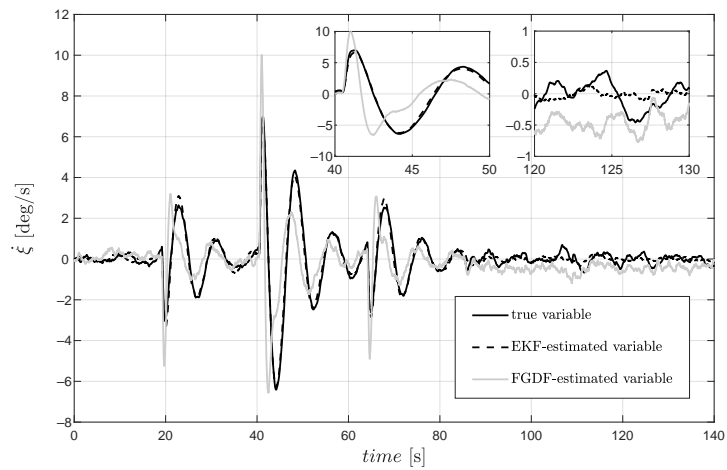


Figure 14. Comparison between the true and the estimated swing rate $\dot{\zeta}$ (Case 3, no active payload stabilization).

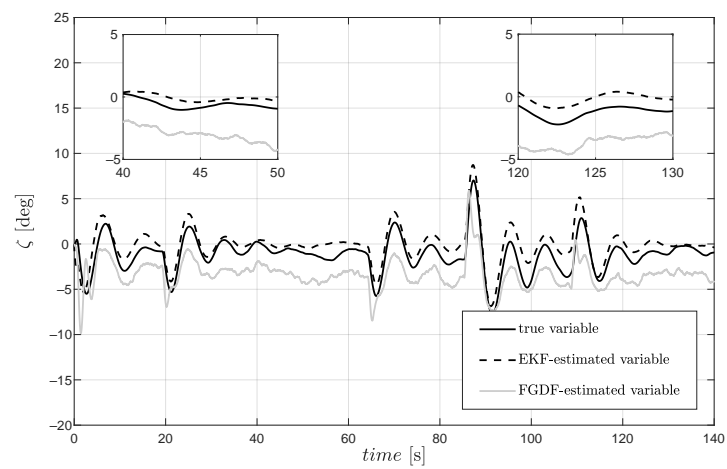


Figure 15. Comparison between the true and the estimated swing angle ζ (Case 3, no active payload stabilization).

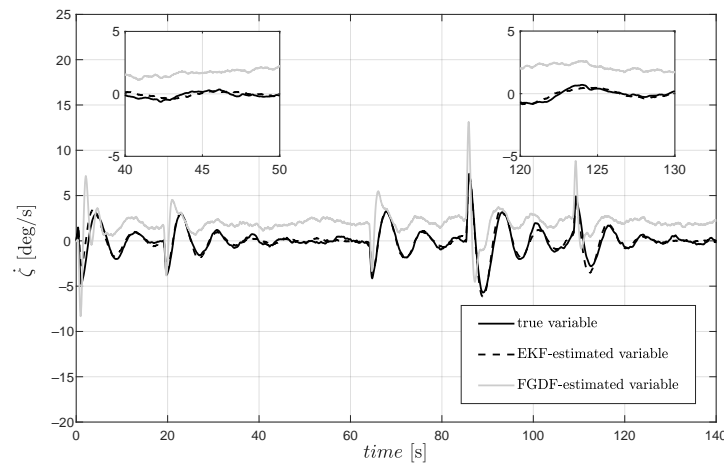


Figure 16. Comparison between the true and the estimated swing rate $\dot{\zeta}$ (Case 3, no active payload stabilization).

In the case when PC is activated based on FGDF information, the mission is performed with indicators listed in the fourth column of Table 5. Despite the macroscopic drawbacks of the FGD approach highlighted through Figures 13–16, active payload stabilization still shows to be a successful strategy (although with degraded results in terms of $\bar{\chi}$ and \bar{v}).

4.2. Experimental Results

In order to evaluate the proposed method in a real mission scenario, an experimental campaign is performed by using a Holybro PX4 Development Kit X500 V2 quadrotor with take-off mass $m = 2$ kg and a wheelbase of 0.5 m (see Figure 17a). The avionics is represented by a Pixhawk[®] 6X Autopilot Flight Controller with M8N GPS. The propulsion system is made of 4 BLHeli S ESC 20A compatible with 4S Li-Po Battery, 4 Holybro 2216 KV920 motors, and a planar set of 1045 propellers. The vehicle is equipped with a thin woven rope with nominal length $L = 1.9$ m, suspended by a hook positioned 0.22 m below the quadrotor top surface ($STA_H = BL_H = 0$ m and $WL_H = -0.22$ m, see Figure 17b). The hook is fixed to a two-axis potentiometer system whose signals, sampled at 20 Hz, are acquired by the onboard computer, converted to angles relative to \mathcal{F}_B , and corrected by quadrotor attitude information to provide direct measurement of oscillation angles ξ and ζ with respect to the local frame \mathcal{F}_H . The payload is a ball with radius 0.03 m and mass $m_l = 0.192$ kg.



Figure 17. (a) Quadcopter used for the experimental campaign; (b) the 2-axis potentiometer system.

Flight tests are performed outdoors with an environmental temperature of 8 °C and a static pressure of 1020 hPa in the presence of light-unsteady 30 deg NE wind. The quadrotor is piloted by imposing desired speed components expressed in \mathcal{F}_H and a desired yaw angle through the remote controller. The EKF and the FGDF algorithms run simultaneously on the Pixhawk device with a frequency of 100 Hz, and no active payload

stabilization is performed. With respect to the EKF algorithm, estimated covariance matrix is initialized with $P_0 = \text{diag}(2.2 \cdot 10^{-5}, 2.2 \cdot 10^{-5}, 1.3 \cdot 10^{-4}, 1.3 \cdot 10^{-4}, 4.3 \cdot 10^{-5}, 4.3 \cdot 10^{-5}, 4.3 \cdot 10^{-5})$, and the assigned noise covariance matrix is $R = 3.6 \cdot 10^{-5} \cdot I_3 \text{ m}^2/\text{s}^4$ (the same adopted in Section 4.1). The numerical integration of Equations (10) and (12) is performed through a discrete backward Euler method [36]. With respect to the FGDF algorithm, it is $R^{(FGDF)} = 2.465 \cdot 10^{-4} \cdot I_2 \text{ rad}^2$ and $(E^-)^{(FGDF)}_0 = \text{diag}(2.2 \cdot 10^{-5}, 2.2 \cdot 10^{-5}, 1.3 \cdot 10^{-4}, 1.3 \cdot 10^{-4})$, while the state transition matrix and the control-input models are, respectively

$$\Phi = \begin{bmatrix} 1 & 0 & 0.01 & 0 \\ 0 & 1 & 0 & 0.01 \\ -0.057 & 0 & 1 & 0 \\ 0 & -0.057 & 0 & 1 \end{bmatrix}, \quad \Gamma = 10^{-3} \cdot \begin{bmatrix} 0 & 0.013 \\ -0.013 & 0 \\ 0 & 2.64 \\ -2.64 & 0 \end{bmatrix} \quad (26)$$

Both filters are initialized with null state and the parameters that optimize estimation performance are, respectively, $\beta_T = 0.996$ (FGDF) and $Q = \text{diag}(1, 1, 2, 2, 1, 1, 1) \cdot 10^{-5}$ (EKF), obtained after an intensive experimental campaign.

In Figure 18, a first maneuver (Maneuver 1) is described where the quadrotor is required to track a desired lateral speed of $\pm 3 \text{ m/s}$ along y_H with a hovering flight phase in between. A lateral payload oscillation is excited according to Figure 19a, where the time history of lateral oscillation angle is reported. The corresponding angular rate is plotted in Figure 19b after numerical derivation and low-pass filtering of potentiometer readings. EKF-based data show very good agreement with direct measurements in all phases, with some over-estimation tendency during transients. FGDF-based data result to be less accurate with a biased behavior that becomes evident when the quadrotor is stabilized in the hovering condition and even deteriorates when negative lateral speed is achieved. During the maneuver, a disturbance force is observed with values projected over the local horizontal plane equal to -1.5 N and -0.7 N on average, respectively, rotated back to x_E and y_E . Such results are compatible with the observed direction of wind.

In Figures 20 and 21, a second maneuver (Maneuver 2) is described to specifically excite headwind payload oscillations. Stabilization of speed along x_H is represented in Figure 20, where the quadrotor starts from a non-nominal hovering condition with residual payload oscillations ($440 \leq t \leq 468 \text{ s}$) and is then required to track a time-dependent speed profile between -2 and $+3 \text{ m/s}$ ($t > 468 \text{ s}$). Satisfactory performance characterizes EKF results during the entire maneuver, according to Figure 21. With regard to FGDF data, acceptable results are obtained during the first phase, despite an evident overestimation of ζ angle near hover. Performance is evidently degraded during the final high-agility maneuver.

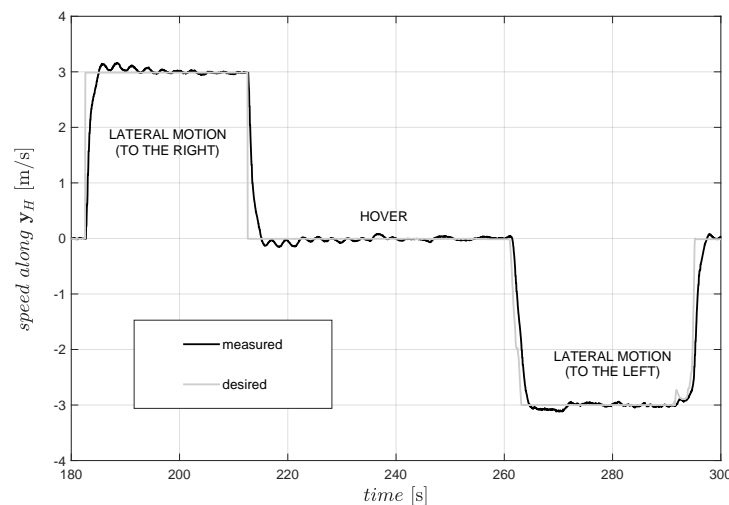


Figure 18. Maneuver 1: stabilization of quadrotor lateral speed.

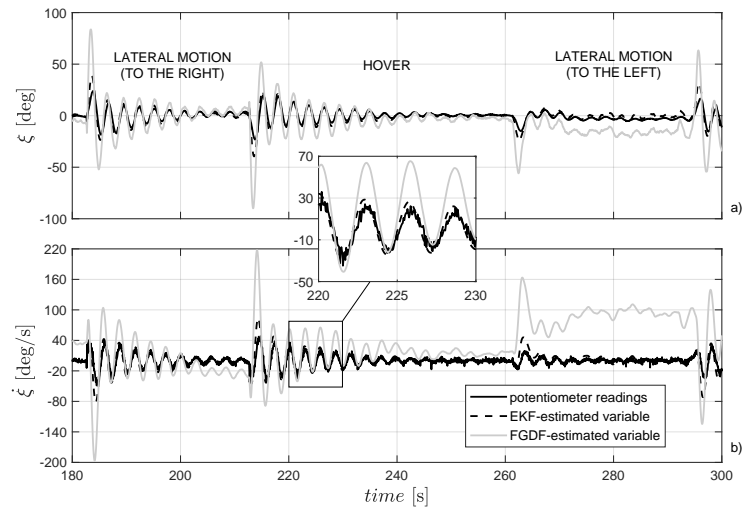


Figure 19. Maneuver 1: comparison between potentiometer readings and filter-estimated data (lateral swing).

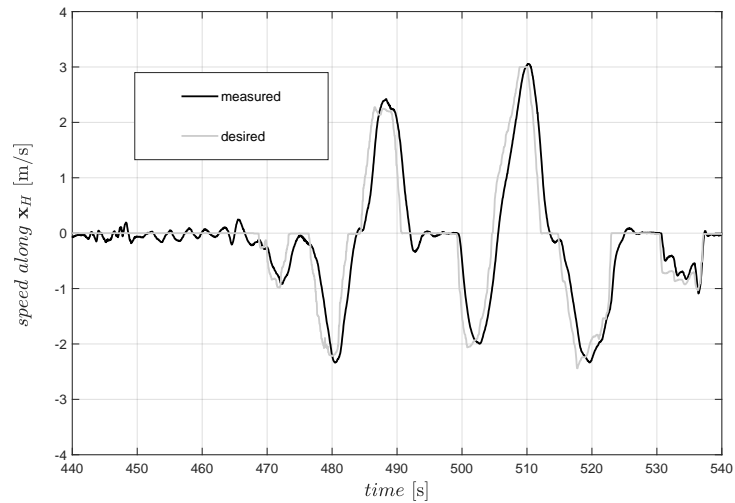


Figure 20. Maneuver 2: stabilization of quadrotor longitudinal speed.

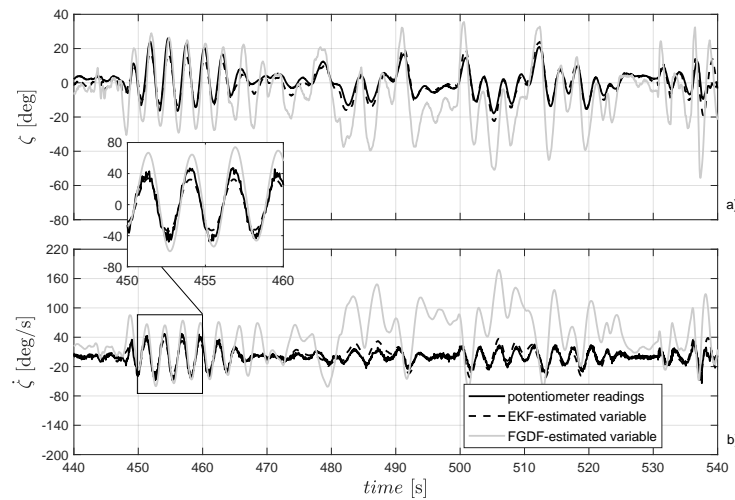


Figure 21. Maneuver 2: comparison between potentiometer readings and filter-estimated data (frontal swing).

5. Conclusions

In the present paper, an estimation algorithm is proposed to characterize the swing state of a suspended load carried by a multirotor drone. The approach is based on a recursive Kalman formulation where vehicle acceleration measurements are fused with model information in a nonlinear framework. Equations are derived for a double point mass system with a mass-less and rigid cable. Numerical simulations demonstrate the validity of the approach in a realistic scenario, where a highly nonlinear octarotor vehicle is analyzed in the presence of system uncertainties, external disturbances, and cable elasticity. The nonlinearity of the approach and the possibility to estimate and compensate external disturbances make the filter suitable for inclusion in a closed-loop stabilization framework, where active oscillation damping is shown to determine the reduction in both maneuver time and battery power consumption.

The proposed algorithm is implemented in a real quadrotor platform and an outdoor experimental campaign is performed to address the accuracy of estimation and demonstrate improved performance with respect to that obtainable through a recent work by one of the authors. The approach has the merit of relative simplicity and can be extended for application to any rotorcraft configuration with minimum effort. The results obtained by both numerical and experimental tests prove to be encouraging for future drone delivery scenarios where the adoption of auxiliary instrumentations or ad hoc indoor facilities is not considered.

Author Contributions: Conceptualization, E.L.d.A.; methodology, E.L.d.A. and F.G.; software, E.L.d.A.; validation, E.L.d.A. and F.G.; formal analysis, E.L.d.A. and F.G.; investigation, E.L.d.A. and F.G.; resources, E.L.d.A. and F.G.; data curation, E.L.d.A. and F.G.; writing—original draft preparation, E.L.d.A.; writing—review and editing, E.L.d.A. and F.G.; visualization, E.L.d.A. and F.G.; supervision, E.L.d.A. and F.G.; project administration, F.G.; funding acquisition, F.G. All authors have read and agreed to the published version of the manuscript.

Funding: This study was carried out within the MOST—Sustainable Mobility National Research Center and received funding from the European Union Next-GenerationEU (PIANO NAZIONALE DI RIPRESA E RESILIENZA (PNRR)—MISSIONE 4 COMPONENTE 2, INVESTIMENTO 1.4—D.D. 1033 17/06/2022, CN00000023). This manuscript reflects only the authors' views and opinions; neither the European Union nor the European Commission can be considered responsible for them.

Data Availability Statement: Data sharing not applicable

Acknowledgments: The authors wish to express their sincerest gratitude to Zephyr S.r.l. for the effective cooperation that allowed the performance of the experimental campaign.

Conflicts of Interest: The authors declare no conflicts of interest.

Appendix A. EKF Jacobian Components

In what follows, filter recursive equations introduced in Section 3 are detailed. In particular, the non-null components of state transition matrix $F(t)$ and observation matrix $H(t)$ are listed, according to Equations (8) and (9), and the definitions in Equation (13):

$$F_{13} = F_{24} = 1 \quad (A1)$$

$$F_{31} = (u_3 \cos x_1 + x_7 \cos x_1 - u_2 \sin x_1 - x_6 \sin x_1) / (L m \cos x_2) \quad (A2)$$

$$F_{32} = 2 x_3 x_4 + [\sin x_2 (u_2 \cos x_1 + x_6 \cos x_1 + u_3 \sin x_1 + x_7 \sin x_1 + 2 L m x_3 x_4 \sin x_2)] / (L m \cos^2 x_2) \quad (A3)$$

$$F_{33} = 2 x_4 \tan x_2 \quad (\text{A4})$$

$$F_{34} = 2 x_3 \tan x_2 \quad (\text{A5})$$

$$F_{36} = \cos x_1 / (L m \cos x_2) \quad (\text{A6})$$

$$F_{37} = \sin x_1 / (L m \cos x_2) \quad (\text{A7})$$

$$F_{41} = -\sin x_2 [(u_2 + x_6) \cos x_1 + (u_3 + x_7) \sin x_1] / (L m) \quad (\text{A8})$$

$$F_{42} = (u_1 \sin x_2 + x_5 \sin x_2 + L m x_3^2 + u_3 \cos x_1 \cos x_2 + x_7 \cos x_1 \cos x_2 - u_2 \cos x_2 \sin x_1 - x_6 \cos x_2 \sin x_1 - 2 L m x_3^2 \cos^2 x_2) / (L m) \quad (\text{A9})$$

$$F_{43} = -x_3 \sin(2 x_2) \quad (\text{A10})$$

$$F_{45} = -\cos x_2 / (L m) \quad (\text{A11})$$

$$F_{46} = -\sin x_1 \sin x_2 / (L m) \quad (\text{A12})$$

$$F_{47} = \cos x_1 \sin x_2 / (L m) \quad (\text{A13})$$

$$H_{11} = m_l \sin(2 x_2) [(u_2 + x_6) \cos x_1 + (u_3 + x_7) \sin x_1] / (2 m M) \quad (\text{A14})$$

$$H_{12} = -m_l [u_1 \sin(2 x_2) + x_5 \sin(2 x_2) - u_3 \cos x_1 - x_7 \cos x_1 + u_2 \sin x_1 + x_6 \sin x_1 + 2 u_3 \cos x_1 \cos^2 x_2 + 2 x_7 \cos x_1 \cos^2 x_2 - 2 u_2 \cos^2 x_2 \sin x_1 - 2 x_6 \cos^2 x_2 \sin x_1 - 3 L m x_3^2 \cos^3 x_2 + 2 L m x_3^2 \cos x_2 - L m x_4^2 \cos x_2] / (m M) \quad (\text{A15})$$

$$H_{13} = 2 L m_l x_3 (\sin x_2 - \sin^3 x_2) / M \quad (\text{A16})$$

$$H_{14} = 2 L m_l x_4 \sin x_2 / M \quad (\text{A17})$$

$$H_{15} = (m + m_l \cos^2 x_2) / (m M) \quad (\text{A18})$$

$$H_{16} = m_l \cos x_2 \sin x_1 \sin x_2 / (m M) \quad (\text{A19})$$

$$H_{17} = -m_l \cos x_1 \cos x_2 \sin x_2 / (m M) \quad (\text{A20})$$

$$\begin{aligned}
H_{21} = & -m_l \cos x_2 (u_3 \cos x_2 + x_7 \cos x_2) \\
& - u_1 \cos x_1 \sin x_2 - x_5 \cos x_1 \sin x_2 \\
& - 2 u_3 \cos^2 x_1 \cos x_2 \\
& - 2 x_7 \cos^2 x_1 \cos x_2 \\
& + 2 u_2 \cos x_1 \cos x_2 \sin x_1 \\
& + 2 x_6 \cos x_1 \cos x_2 \sin x_1 \\
& + L m x_4^2 \cos x_1 \\
& + L m x_3^2 \cos x_1 \cos^2 x_2) / (m M)
\end{aligned} \tag{A21}$$

$$\begin{aligned}
H_{22} = & -m_l [u_1 \sin x_1 - x_6 \sin(2 x_2) \\
& - u_2 \sin(2 x_2) + x_5 \sin x_1 \\
& - 2 u_1 \cos^2 x_2 \sin x_1 \\
& - 2 x_5 \cos^2 x_2 \sin x_1 \\
& + 2 u_2 \cos^2 x_1 \cos x_2 \sin x_2 \\
& + 2 x_6 \cos^2 x_1 \cos x_2 \sin x_2 \\
& + 2 u_3 \cos x_1 \cos x_2 \sin x_1 \sin x_2 \\
& + 2 x_7 \cos x_1 \cos x_2 \sin x_1 \sin x_2 \\
& - L m x_4^2 \sin x_1 \sin x_2 \\
& + 3 L m x_3^2 \sin x_1 \sin x_2 \\
& \cdot (\sin^2 x_2 - 1)] / (m M)
\end{aligned} \tag{A22}$$

$$H_{23} = -2 L m_l x_3 \cos^3 x_2 \sin x_1 / M \tag{A23}$$

$$H_{24} = -2 L m_l x_4 \cos x_2 \sin x_1 / M \tag{A24}$$

$$H_{25} = m_l \cos x_2 \sin x_1 \sin x_2 / (m M) \tag{A25}$$

$$\begin{aligned}
H_{26} = & (m + m_l - m_l \cos^2 x_2 \\
& + m_l \cos^2 x_1 \cos^2 x_2) / (m M)
\end{aligned} \tag{A26}$$

$$H_{27} = (m_l \cos x_1 \cos^2 x_2 \sin x_1) / (m M) \tag{A27}$$

$$\begin{aligned}
H_{31} = & [m_l \cos x_2 (u_1 \sin x_1 \sin x_2 \\
& - x_6 \cos x_2 - u_2 \cos x_2 \\
& + x_5 \sin x_1 \sin x_2 + 2 u_2 \cos^2 x_1 \cos x_2 \\
& + 2 x_6 \cos^2 x_1 \cos x_2 \\
& + 2 u_3 \cos x_1 \cos x_2 \sin x_1 \\
& + 2 x_7 \cos x_1 \cos x_2 \sin x_1 \\
& - L m x_4^2 \sin x_1 \\
& - L m x_3^2 \cos^2 x_2 \sin x_1)] / (m M)
\end{aligned} \tag{A28}$$

$$\begin{aligned}
H_{32} = & -[m_l \cos x_1 (2 u_1 \cos^2 x_2 - x_5 \\
& - u_1 + 2 x_5 \cos^2 x_2 + L m x_4^2 \sin x_2 \\
& - 2 u_3 \cos x_1 \cos x_2 \sin x_2 \\
& - 2 x_7 \cos x_1 \cos x_2 \sin x_2 \\
& + 2 u_2 \cos x_2 \sin x_1 \sin x_2 \\
& + 2 x_6 \cos x_2 \sin x_1 \sin x_2 \\
& + 3 L m x_3^2 \cos^2 x_2 \sin x_2)] / (m M)
\end{aligned} \tag{A29}$$

$$H_{33} = 2 L m_l x_3 \cos x_1 \cos^3 x_2 / M \tag{A30}$$

$$H_{34} = 2 L m_l x_4 \cos x_1 \cos x_2 / M \tag{A31}$$

$$H_{35} = -m_l \cos x_1 \cos x_2 \sin x_2 / (m M) \tag{A32}$$

$$H_{36} = m_l \cos x_1 \cos^2 x_2 \sin x_1 / (m M) \tag{A33}$$

$$H_{37} = (M - m_l \cos^2 x_1 \cos^2 x_2) / (m M) \tag{A34}$$

References

1. Pounds, P.E.I.; Bersak, D.R.; Dollar, A.M. Grasping From the Air: Hovering Capture and Load Stability. In Proceedings of the IEEE International Conference on Robotics and Automation, Shanghai, China, 9–13 May 2011; pp. 2491–2498. [\[CrossRef\]](#)
2. Chen, H.; Quan, F.; Fang, L.; Zhang, S. Aerial Grasping with a Lightweight Manipulator Based on Multi-Objective Optimization and Visual Compensation. *Sensors* **2019**, *19*, 4253. [\[CrossRef\]](#) [\[PubMed\]](#)
3. Eskandaripour, H.; Boldsai Khan, E. Last-Mile Drone Delivery: Past, Present, and Future. *Drones* **2023**, *7*, 77. [\[CrossRef\]](#)
4. Li, X.; Zhang, J.; Han, J. Trajectory planning of load transportation with multi-quadrotors based on reinforcement learning algorithm. *Aerosp. Sci. Technol.* **2021**, *116*, 106887. [\[CrossRef\]](#)
5. Pounds, P.; Bersak, D.; Dollar, A. Stability of small-scale UAV helicopters and quadrotors with added payload mass under PID control. *Auton. Robot.* **2012**, *33*, 129–142. [\[CrossRef\]](#)
6. Palunko, I.; Fierro, R.; Cruz, P. Trajectory generation for swing-free maneuvers of a quadrotor with suspended payload: A dynamic programming approach. In Proceedings of the IEEE International Conference on Robotics and Automation, Saint Paul, MN, USA, 14–18 May 2012; pp. 2691–2697. [\[CrossRef\]](#)
7. Dai, S.; Lee, T.; Bernstein, D.S. Adaptive Control of a Quadrotor UAV Transporting a Cable-Suspended load with Unknown Mass. In Proceedings of the the 53rd Conference on Decision and Control (CDC), Los Angeles, CA, USA, 15–17 December 2014; pp. 6149–6154. [\[CrossRef\]](#)
8. Sreenath, K.; Lee, T.; Kumar, V. Geometric control and differential flatness of a quadrotor UAV with a cable-suspended load. In Proceedings of the the 52nd IEEE Conference on Decision and Control (CDC), Firenze, Italy, 10–13 December 2013; pp. 2269–2274. [\[CrossRef\]](#)
9. Nicotra, M.M.; Garone, E.; Naldi, R.; Marconi, L. Nested saturation control of an UAV carrying a suspended load. In Proceedings of the the American Control Conference, Portland, OR, USA, 4–6 June 2014; pp. 3585–3590. [\[CrossRef\]](#)
10. Pizetta, I.H.B.; Brandão, A.S.; Sarcinelli-Filho, M. Modelling and control of a PVTOL quadrotor carrying a suspended load. In Proceedings of the the International Conference on Unmanned Aircraft Systems (ICUAS), Denver, CO, USA, 9–12 June 2015; pp. 444–450. [\[CrossRef\]](#)
11. Potter, J.; Singhose, W.; Costelloy, M. Reducing swing of model helicopter sling load using input shaping. In Proceedings of the 9th IEEE International Conference on Control and Automation (ICCA), Santiago, Chile, 19–21 December 2011; pp. 348–353. [\[CrossRef\]](#)
12. Bingöl, Ö.; Güzey, H.M. Finite-Time Neuro-Sliding-Mode Controller Design for Quadrotor UAVs Carrying Suspended Payload. *Drones* **2022**, *6*, 311. [\[CrossRef\]](#)
13. Outeiro, P.; Cardeira, C.; Oliveira, P. Control Architecture for a Quadrotor Transporting a Cable-Suspended Load of Uncertain Mass. *Drones* **2023**, *7*, 201. [\[CrossRef\]](#)
14. de Angelis, E.L.; Giulietti, F.; Pipeleers, G. Two-time-scale control of a multirotor aircraft for suspended load transportation. *Aerosp. Sci. Technol.* **2019**, *84*, 193–203. [\[CrossRef\]](#)
15. de Angelis, E.L.; Giulietti, F. Stability and control issues of multirotor suspended load transportation: An analytical closed-form approach. *Aerosp. Sci. Technol.* **2023**, *135*, 108201. [\[CrossRef\]](#)
16. Guerrero-Sánchez, M.E.; Hernández-González, O.; Lozano, R.; Garcia-Beltrán, C.D.; Valencia-Palomo, G.; López-Estrada, F.R. Energy-Based Control and LMI-Based Control for a Quadrotor Transporting a Payload. *Mathematics* **2019**, *7*, 1090. [\[CrossRef\]](#)

17. Mohiuddin, A.; Taha, T.; Zweiri, Y.; Gan, D. UAV Payload Transportation via RTDP Based Optimized Velocity Profiles. *Energies* **2019**, *12*, 3049. [[CrossRef](#)]
18. Cabecinhas, D.; Cunha, R.; Silvestre, C. A trajectory tracking control law for a quadrotor with slung load. *Automatica* **2019**, *106*, 384–389. [[CrossRef](#)]
19. Wang, T.; Zhou, J.; Wu, Z.; Liu, R.; Zhang, J.; Liang, Y. A Time-Varying PD Sliding Mode Control Method for the Container Crane Based on a Radial-Spring Damper. *Electronics* **2022**, *11*, 3543. [[CrossRef](#)]
20. How, J.P.; Behnhke, B.; Frank, A.; Dale, D.; Vian, J. Realtime indoor autonomous vehicle test environment. *IEEE Control Syst.* **2008**, *28*, 51–64. [[CrossRef](#)]
21. Lupashin, S.; Hehn, M.; Mueller, M.W.; Schoellig, A.P.; Sherback, M.; D’Andrea, R. A platform for aerial robotics research and demonstration: The flying machine arena. *Mechatronics* **2014**, *24*, 41–54. [[CrossRef](#)]
22. Zürn, M.; Morton, K.; Heckmann, A.; McFadyen, A.; Notter, S.; Gonzalez, F. MPC controlled multirotor with suspended slung load: System architecture and visual load detection. In Proceedings of the IEEE Aerospace Conference, Big Sky, MT, USA, 5–12 March 2016; pp. 1–11. [[CrossRef](#)]
23. Ebrahimi, M.; Ghayour, M.; Madani, S.M.; Khoobroo, A. Swing angle estimation for anti-sway overhead crane control using load cell. *Int. J. Control Autom. Syst.* **2011**, *9*, 301–309. [[CrossRef](#)]
24. Feng, Y.; Wang, J. GPS RTK Performance Characteristics and Analysis. *J. Glob. Position Syst.* **2008**, *7*, 1–8. [[CrossRef](#)]
25. Kim, Y.S.; Hong, K.S.; Sul, S.K. Anti-Sway Control of Container Cranes: Inclinometer, Observer, and State Feedback. *Int. J. Control Autom. Syst.* **2004**, *2*, 435–449. [[CrossRef](#)]
26. Paul, H.; Ono, K.; Ladig, R.; Shimonomura, K. A Multirotor Platform Employing a Three-Axis Vertical Articulated Robotic Arm for Aerial Manipulation Tasks. In Proceedings of the IEEE/ASME International Conference on Advanced Intelligent Mechatronics (AIM), Auckland, New Zealand, 9–12 July 2018; pp. 478–485. [[CrossRef](#)]
27. Lee, S.J.; Kim, H.J. Autonomous Swing-Angle Estimation for Stable Slung-Load Flight of Multi-Rotor UAVs. In Proceedings of the IEEE International Conference on Robotics and Automation (ICRA), Singapore, 29 May–3 June 2017; pp. 4576–4581. [[CrossRef](#)]
28. de Angelis, E.L. Swing angle estimation for multicopter slung load applications. *Aerosp. Sci. Technol.* **2019**, *89*, 264–274. [[CrossRef](#)]
29. de Angelis, E.L.; Ferrarese, G.; Giulietti, F.; Modenini, D.; Tortora, P. Terminal height estimation using a Fading Gaussian Deterministic filter. *Aerosp. Sci. Technol.* **2016**, *55*, 366–376. [[CrossRef](#)]
30. Lee, S.; Son, H. Antisway Control of a Multirotor With Cable-Suspended Payload. *IEEE Trans. Control Syst. Technol.* **2021**, *29*, 2630–2638. [[CrossRef](#)]
31. de Angelis, E.L.; Giulietti, F.; Pipeleers, G.; Rossetti, G.; Van Parys, R. Optimal autonomous multirotor motion planning in an obstructed environment. *Aerosp. Sci. Technol.* **2019**, *87*, 379–388. [[CrossRef](#)]
32. Talbot, P.D.; Tinling, B.E.; Decker, W.A.; Chen, R.T.N. *A Mathematical Model of a Single Main Rotor Helicopter for Piloted Simulation*; NASA Technical Memorandum 84281; NASA: Washington, DC, USA, 1982; pp. 1–52.
33. Leishman, J.G. *Principles of Helicopter Aerodynamics*, 2nd ed.; Cambridge University Press: New York, NY, USA, 2006; Chapters 2 and 5.
34. Stevens, B.L.; Lewis, F.L.; Johnson, E.N. *Aircraft Control and Simulation: Dynamics, Controls Design, and Autonomous Systems*, 3rd ed.; Wiley-Blackwell: Hoboken, NJ, USA, 2015; Chapter 1.
35. Brown, R.G.; Hwang, P.Y.C. *Introduction to Random Signals and Applied Kalman Filtering*, 3rd ed.; John Wiley & Sons: New York, NY, USA, 1997; pp. 289–293.
36. Butcher, J.C. Numerical methods for ordinary differential equations in the 20th century. *J. Comput. Appl. Math.* **2000**, *125*, 1–29. [[CrossRef](#)]
37. Kim, H.W.; Brown, R.E. A Comparison of Coaxial and Conventional Rotor Performance. *J. Am. Helicopter. Soc.* **2010**, *55*, 012004. [[CrossRef](#)]
38. Forsythe, G.E.; Malcolm, M.A.; Moler, C.B. *Computer Methods for Mathematical Computations*; Prentice-Hall: Hoboken, NJ, USA 1976; Chapter 7.
39. NOAA-S/T 76-1562; U.S. Standard Atmosphere. U.S. Government Printing Office: Washington, DC, USA, 1976; pp. 1–241.
40. Memon, S.A.; Son, H.; Kim, W.G.; Khan, A.M.; Shahzad, M.; Khan, U. Tracking Multiple Unmanned Aerial Vehicles through Occlusion in Low-Altitude Airspace. *Drones* **2023**, *7*, 241. [[CrossRef](#)]
41. PX4 Development Team and Community, PX4 Autopilot User Guide (Main). Available online: <https://docs.px4.io/main/en/> (accessed 20 September 2023).
42. Ho, D.; Linder, J.; Hendeby, G.; Enqvist, M. Vertical modeling of a quadcopter for mass estimation and diagnosis purposes. In Proceedings of the 2017 Workshop on Research, Education and Development of Unmanned Aerial Systems (RED-UAS), Linköping, Sweden, 3–5 October 2017; pp. 192–197. [[CrossRef](#)]
43. Fraser, C.T.; Ulrich, S. Adaptive extended Kalman filtering strategies for spacecraft formation relative navigation. *Acta Astronaut.* **2021**, *178*, 700–721. [[CrossRef](#)]
44. Hakim, T.M.I.; Arifianto, O. Implementation of Dryden Continuous Turbulence Model into Simulink for LSA-02 Flight Test Simulation. *J. Phys. Conf. Ser.* **2018**, *1005*, 012017. [[CrossRef](#)]
45. U.S. Department of Defense. *Flying Qualities of Piloted Airplanes, U.S. Military Specification MIL-F-8785C*; U.S. Department of Defense: Washington, VA, USA, 1980; pp. 1–95.

46. U.S. Department of Defense. *Flying Qualities of Piloted Aircraft, U.S. Military Handbook MIL-HDBK-1797B*; U.S. Department of Defense: Washington, VA, USA, 2012; pp. 1–849.
47. Higham, N.J. The Scaling and Squaring Method for the Matrix Exponential Revisited. *SIAM J. Matrix Anal. Appl.* **2005**, *26*, 1179–1193. [[CrossRef](#)]

Disclaimer/Publisher’s Note: The statements, opinions and data contained in all publications are solely those of the individual author(s) and contributor(s) and not of MDPI and/or the editor(s). MDPI and/or the editor(s) disclaim responsibility for any injury to people or property resulting from any ideas, methods, instructions or products referred to in the content.